Peruzzetto, M., Levy, C., Thiery, Y., Grandjean, G., Mangeney, A., Lejeune, A.-M., Nachbaur, A., Legendre, Y., Vittecoq, B., Saurel, J.-M., Clouard, V., Dewez, T., Fontaine, F. R., Mergili, M., Lagarde, S., Komorowski, J.-C., Le Friant, A., Lemarchand, A. (2022): Simplified simulation of rock avalanches and subsequent debris flows with a single thin-layer model: Application to the Prêcheur river (Martinique, Lesser Antilles). - Engineering Geology, 296, 106457.

https://doi.org/10.1016/j.enggeo.2021.106457

Simplified simulation of rock avalanches and subsequent debris flows with a single thin-layer model. Application to the Prêcheur river (Martinique, Lesser Antilles)

Marc Peruzzetto[1, 2], Clara Levy[2], Yannick Thiery[2], Gilles Grandjean[2], Anne Mangeney[1], Anne-Marie Lejeune[1,3], Aude Nachbaur[4], Yoann Legendre[5], Benoit Vittecoq[4], Jean-Marie Saurel[1], Valérie Clouard[6], Thomas Dewez[2], Fabrice R. Fontaine[1,3], Martin Mergili[7], Sophie Lagarde[1,8], Jean-Christophe Komorowski[1], Anne Le Friant[1], and Arnaud Lemarchand[1]

[1]Université de Paris, Institut de physique du globe de Paris, CNRS, F-75005 Paris, France

[2]BRGM, Orléans, France

[3]Observatoire volcanologique et sismologique de la Martinique, Institut de physique du globe de Paris, F-97250 Fonds Saint Denis, France.

[4]BRGM Martinique, 7200 Fort-de-France, France

[5]BRGM Guadeloupe, 97170 Petit-Bourg, France

[6]GET/OMP - UMR 5563 CNRS - UM 97 UPS - UR 234 IRD - CNES, Toulouse, France

[7]Institute of Geography and Regional Science, University of Graz, Graz, Austria

[8]Section 4.6 Geomorphology, GFZ German Research Centre for Geosciences, Postdam, Germany

ABSTRACT

High discharge debris flows in mountainous and volcanic areas are major threats to populations and infrastructures. Modeling such events is challenging because the associated processes are complex, and because we often lack data to constrain rheological parameters. In this work, we show how the extensive use of field data can help model a rock avalanche, and the subsequent remobilization of the deposits as a high discharge debris flow, with a single one-phase thin-layer numerical code, SHALTOP, and up to two rheological parameters. With the Prêcheur river catchment (Martinique, Lesser Antilles) as a case study, we use geological and geomorphological data, topographic surveys, seismic recordings and granulometric analyses to define realistic simulation scenarios and determine the main characteristics of documented events for model calibration. Then, we model a possible 1.9×10^6 m^3 rock avalanche. The resulting deposits are remobilized instantaneously as a high discharge debris flow. We show that, for a given unstable volume, successive collapses allow to better reproduce the dynamics of the rock avalanche, but do not change the geometry of the final deposits, and thus the initial conditions of the subsequent debris flow simulation. The location of the debris flow initiation has also little influence on simulation results. However, progressive remobilization of materials slows down the debris flow and limits overflows, in comparison to an instantaneous release. Nevertheless, high discharge debris flows are well reproduced with an instantaneous initiation. Besides, the range of travel times measured for other significant debris flows in the Prêcheur river is consistent with our simulation results.

Keywords: landslide, lahar, debris flow, modeling, thin-layer

Highlights

- Successful mass flow simulations with up to two rheological parameters
- Extensive use of field data for model calibration and scenario definition
- Mapping of areas exposed to high discharge debris flow, for hazard assessment

1 INTRODUCTION

The remobilization by water of old or recent volcanic materials, during or even long after an eruption, generates sediment-laden flows called lahars that travel in ravines and rivers tens to hundreds of kilometers away from the volcano (Vallance and Iverson, 2015; Thouret et al., 2020). Thus, they can be major threats to populations and infrastructures. Non-eruptive lahars can be correlated to landslides that create loose debris reservoirs. Numerical simulations considering both the landslide that creates the reservoir and its remobilization as lahars can improve hazard assessment. However, the modeling process is not straight-forward because the initial landslide and the subsequent lahar are two different phenomena.

The initial landslide can take various forms, as water-laden debris avalanches or dry rock avalanches (Hungr et al., 2014). In a first approximation, the physical and rheological properties of materials (such as density or basal friction coefficient) can be considered homogeneous both in space and time, which simplifies the quantification of the propagation (McDougall and Hungr, 2005). In comparison, the subsequent lahars are more complex: they can propagate as hyperconcentrated flows (HFs) or debris flows (DFs). In the following, we will thus talk about lahars to refer to both DFs and HFs. Following (Coussot and Meunier, 1996; Vallance and Iverson, 2015; Thouret et al., 2020), we define DFs as homogeneous mixtures of water and granular rock material with volumetric solid fraction higher than 60%, similar velocities for the solid and fluid phases and densities above 1800 kg m^{-3}. HFs feature solid fractions between 20% and 60%, a vertical separation of the two phases and densities below 1800 kg m^{-3}. We may expect that the remobilization of a small amount of solid materials will produce HFs, while fast remobilization by liquefaction of a large debris reservoir will turn into a DF (Vallance and Iverson, 2015). However, a DF initiated in the upper section of a river may well turn into HF at its tail because of dilution and settling, while its front increases its solid content due to bed erosion. Further dilution downstream can then transform completely the DF into a HF (for a conceptual view of such a process, see Figure 2 in Thouret et al., 2020).

The combined effects of particle collision and friction, lubrication, advection and suspension in presence of an interstitial fluid, are difficult to model in a single framework (Andreotti et al., 2013; Delannay et al., 2017). Thus, current solutions where the dynamics of elementary volumes of fluid and/or of each solid particle are considered (in 2 or 3 dimensions) often focus on reproducing some of the physical processes, but never all of them. Discrete element modeling (DEM) is now widely used to model dry and wet granular flows at the laboratory scale (Durán et al., 2012; Lefebvre-Lepot et al., 2015; Windows-Yule et al., 2016, e.g.). Applications to field scale simulations are given for instance by (Zhao and Shan, 2013) and Leonardi et al. (2014) for DFs, and by Yan et al. (2020) and Wu and Hsieh (2021) for rock avalanches. Another approach is to consider a single-phase flow and solve the Navier-Stokes equations (e.g. Hu et al., 2015). However, both DEM and continuous models often require huge computing resources and/or depend on too many user-defined parameters, which is incompatible with the limited knowledge of the flowing material we have in practice.

Over the past decades, thin-layer models have been increasingly used to study debris and rock avalanches, as well as lahars (see McDougall (2017) for a general review, and Thouret et al. (2020) for lahar modeling). Their main assumption is that the landslide thickness is negligible in comparison to its length. In turn, flow description is reduced to flow thickness and flow thickness-averaged velocity, which simplifies greatly the governing equations in comparison to 3D models. In their simplest form, thin-layer models describe an homogeneous flow and dissipate energy solely by considering a stress applied at the base of the flow. For instance, with the Coulomb rheology the only rheological parameter is the friction coefficient $\mu_S = \tan(\delta)$, with δ the friction angle. If the topographic slope θ is higher than δ the flow accelerates, and decelerates and stops otherwise (inertial effects and spatial variations in flow thickness may change temporarily this first-order behavior). Such models proved to reproduce well rock and debris avalanches as well as debris flows (Hungr et al., 2007; Pirulli and Mangeney, 2008; Favreau et al., 2010; Lucas et al., 2014; Pastor et al., 2018a). More elaborate numerical codes also model, for instance, two-phase flows (Iverson and George, 2014; Bouchut et al., 2015, 2016; Mergili et al., 2017; Pastor et al., 2018b), three-phase flows (fluid, coarse solid fraction, fine solid fraction, Pudasaini and Mergili, 2019), and erosion along flow path (Iverson, 2012; Pirulli and Pastor, 2012). However, these developments often rely on empirical relations (e.g. for erosion laws McDougall, 2017). Besides, thin-layer equations with complex rheologies are mostly derived on simple topographies (e.g. Pastor et al., 2009; Baker et al., 2016), and the lack of analytical solutions makes it difficult to test the robustness of associated numerical tools. Furthermore, although complex rheologies may model more realistic dynamics, they come at the cost of an increased number of parameters, such as erosion rates, erodible thickness, viscosity, drag coefficient or densities of each phase (e.g. George and Iverson, 2014; Mergili et al., 2017). These parameters can be difficult to calibrate if not enough data are available. Besides, when they are not known, the high number of degrees of freedom may artificially improve back-analysis studies.

In practice, experts conducting hazard assessment studies may neither have the time nor the financial resources to carry out a thorough analysis with detailed but complex numerical models. The question is: to what extent can we expect realistic results from simple physically based thin-layer models for rock avalanche and DF simulations? The answer strongly depends on the available field data. In this work, we present a modeling approach with empirical but simple rheologies involving no more than two parameters. To enhance the quality of simulation results, we make an extensive use of field data to define realistic simulation scenarios and characterize past events for model calibration. We will use the thin-layer model SHALTOP (Bouchut et al., 2003; Bouchut and Westdickenberg, 2004; Mangeney-Castelnau et al., 2005; Mangeney et al., 2007b), that proved to reproduce accurately analytical solutions for the dam-break problem (Mangeney et al., 2000; Lucas et al., 2007), and was used successfully to model gravitational flows at the field scale with a simple Coulomb friction law (e.g. Favreau et al., 2010; Lucas et al., 2014; Moretti et al., 2012, 2015; Peruzzetto et al., 2019; Moretti et al., 2020). In comparison to other thin-layer models, SHALTOP also takes into account precisely topography curvature effects that can be significant for fast gravity driven flows (Peruzzetto et al., 2021).

Because they have the highest potential impact on infrastructures and populations, we focus on extreme events (avalanches of volumes $> 1 \times 10^6$ m^3, and high discharge DFs). We choose the Prêcheur river in Martinique island (Lesser Antilles, French Caribbean) as study site (Figure 1), where such events are documented and where stakes are high, as large DFs threaten the Prêcheur village at the mouth of the river (Figure 2). In a first calibration step, we will use topographic surveys and aerial photographs to construct the initial conditions of (i) a rock avalanche that occurred in 2018 and (ii) a major debris flow that occurred in 2010. Granulometric data help choosing the rheological law, and a range of possible rheological parameters is identified in the literature (see Table 1). By reproducing the travel distance and main dynamic characteristics of the rock avalanche, and the flooded area and travel time of the DF (deduced from aerial photographs and seismic recordings in both cases), we calibrate more precisely rheological parameters. With these fine-tuned parameters, we can then consider the forward prediction of a rock avalanche simulation, whose initial conditions are deduced from geomorphological and geological observations. The resulting deposits are then remobilized instantaneously in another simulation to model the propagation of a high discharge DF. Because in the Prêcheur river rock avalanches do not, in general, transform directly into DFs (Aubaud et al., 2013), we do not consider such a continuous transition in this work.

In Section 2 we present in more details our study site, along with the data used to construct simulation scenarios and calibrate our model. Simulation scenarios used for model calibration and forward prediction are presented in Section 3, and the numerical model SHALTOP is detailed in Section 4. Simulation results are then given in Section 5. In Section 6, we investigate the influence of initiation mechanism on simulation results. The latter are discussed in Section 7.

2 DATA

In this section, we present the geological and geomorphological context of our study site, along with the data used to define simulation scenarios. Topographic surveys will be used to define the bed topography and initial volumes. To calibrate the numerical model, we use aerial photographs that give the travel distances and flooded areas of past events. Seismic recordings are used to estimate flow velocity and duration. The granulometry of deposits is also used to choose the rheology in DF simulations. These data are summarized in Table 1.

2.1 Geological context

The Prêcheur river catchment drains part of the western side of Montagne Pelée volcano (Figure 1a). The Samperre cliff is located about 2 km north-west of the volcano summit, at the source of the Samperre river (Figure 2a). Over the past 40 years,

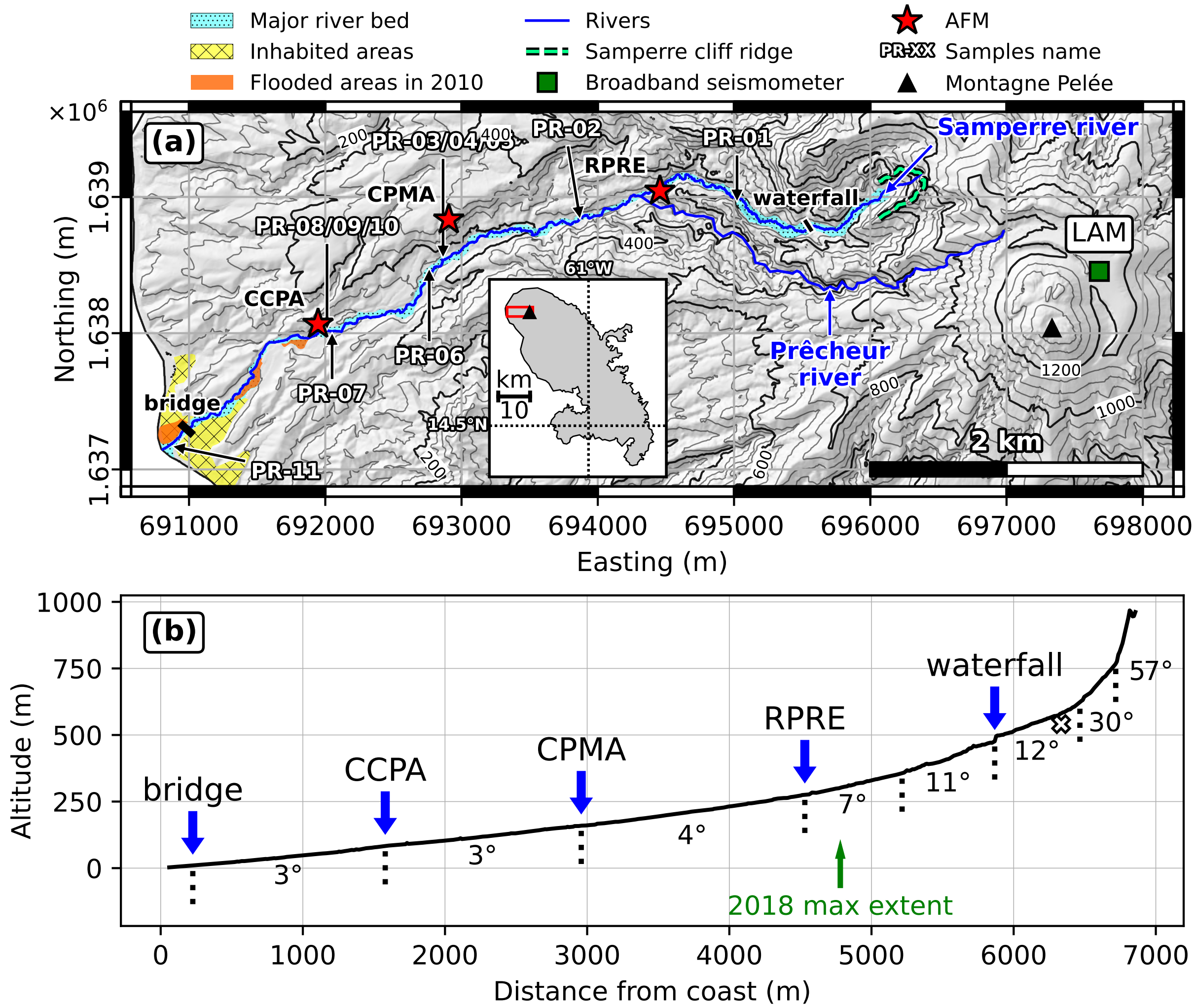

Figure 1. Prêcheur river (Martinique island, Lesser Antilles, French Caribbean) map and section. (a) Map of the Prêcheur river. The insert features the Martinique island, with the red rectangle matching the extent of the map. The 1 m DEM in the river area is from Helimap 08/2018, and from IGN 03/2010 elsewhere. Sampling locations for granulometry analysis are given by black arrows, with corresponding sample names. CCPA, CPMA, RPRE and LAM are the names of AFMs (Acoustic Flow Monitoring) and seismic stations used in this study. Coordinates: WGS84 UTM20N. (b) River cross-section, from the river mouth (left) to the Samperre cliff (right). Green arrow: estimated deposits extents after the 2018 Samperre rock avalanche. White cross: source area for debris flow simulations with imposed discharge (see Sections 6.2 and 6.3). Average slopes are given for each section between dotted vertical black lines. Horizontal and vertical scales differ.

Figure 2. 2018 views of the Samperre cliff and Prêcheur village. (a) Feb. 2, 2018 view of the cliff, after the main rock avalanche of Jan. 4, 2018. The dust cloud generated by a minor collapse is visible on the right side of the cliff. The scree reservoir is highlighted by the black dotted contour. (b) Mar. 30, 2018 helicopter view of the Prêcheur village, constructed on the alluvial fan of the Prêcheur river, with a central view of the bridge.

Table 1. Main characteristics of simulations, derived from literature (citations) and field data (bold).

	Rock avalanche simulation	Debris flow simulation
Topography	08/2018 1-m DEM (modified locally in the Samperre cliff area)	
Initial volume geometry	**07/2010, 01/2018, 08/2018 1-m DEMs** manually modified following - cliff rim evolution (**ORTHO GéoMartinique DEAL February 2007**) - geological / geomorphological observations (Nachbaur et al., 2019)	Difference between **01/2018 and 08/2018 1-m DEMs**
Rheology choice	Coulomb (e.g. Favreau et al., 2010; Lucas et al., 2014; Yamada et al., 2018)	Frictional rheology (**granulometry of deposits**), with Coulomb (Moretti et al., 2015) and Voellmy (McDougall, 2017; Zimmermann et al., 2020)
Range of rheological parameters for calibration	$\tan(\delta) \in [\tan(10°), \tan(20°)] = [0.18, 0.36]$ (Lucas et al., 2014; Peruzzetto et al., 2019)	$\tan(\delta) \in [\tan(2°), \tan(3°)]$ (riverbed slope at the river mouth) $\xi \in [100 \text{ m s}^{-2}, 500 \text{ m s}^{-2}]$ (Zimmermann et al., 2020)
Calibration data	Travel distance (**aerial reconnaissance**) Duration and dynamics (**seismic signal**)	Flooded area (**aerial reconnaissance**) Travel time (**AFMs**)

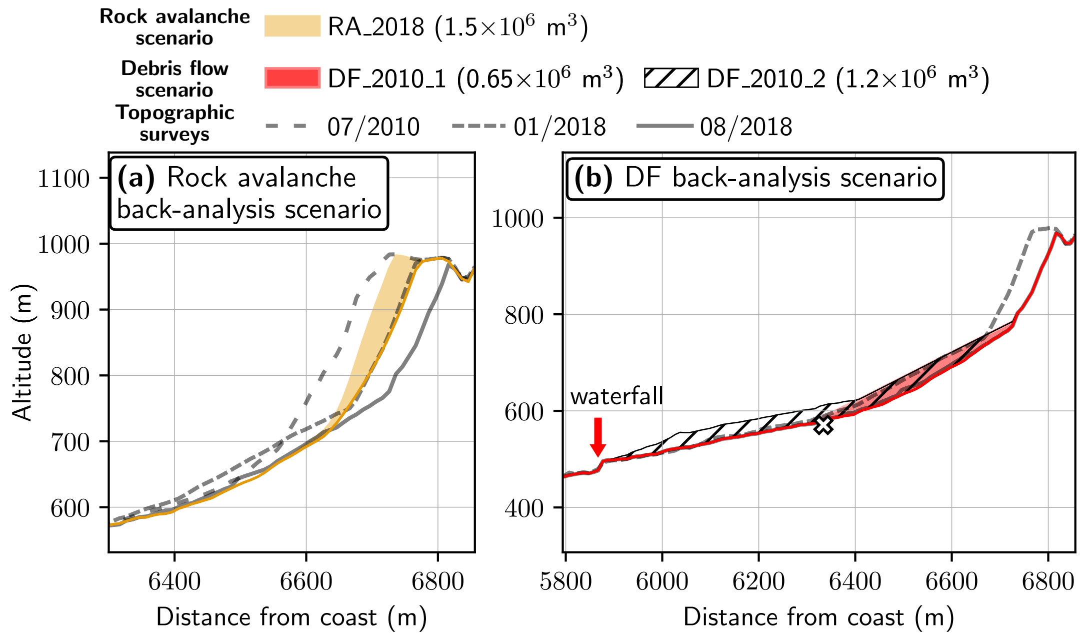

Figure 3. Samperre cliff longitudinal cross-section with topographic surveys and initial mass for calibration scenarios. (a) Successive topographic surveys (gray lines). Orange patch: collapsing volume reconstructed for the *RA_2018* rock avalanche scenario. Orange line: topography in simulation. (b) Initial reservoirs for the *DF_2010_1* and *DF_2010_2* debris flow simulations. White cross: source area for simulation with imposed discharge (see Sections 6.2 and 6.3). Red line: topography in simulation.

the Samperre cliff has produced at least 4 episodes of massive destabilizations in 1980, 1997-1998 (Aubaud et al., 2013), 2009-2011 (2.1×10^6 m^3, Clouard et al., 2013) and 2018-2019 (5×10^6 m^3, Quefféléan, 2018; Nachbaur et al., 2019). However, another collapse episode is inferred from testimonies in the early 1950s (Aubaud et al., 2013). Thus, the cliff rim retreated by 250 m between 1988 and 2018 (Nachbaur et al., 2019). Its evolution between March 2010 and August 2018 is given in Figure 3a (grey lines).

A geological interpretation of the cliff main units is given by Nachbaur et al. (2019) and reproduced in Figure 4a. We will use this interpretation to constrain a potential future cliff collapse (see Table 1 and Table 2). Previous studies (Mathon and Barras, 2010; Clouard et al., 2013; Nachbaur et al., 2019) identified a stable basal layer progressively exposed by successive collapses. This basal layer is composed of old indured volcanic deposits emplaced or exposed during a massive flank collapse 216 kyrs ago (D1 event Le Friant et al., 2003; Boudon et al., 2007; Germa et al., 2011; Brunet et al., 2017), and of old pyroclastic deposits (red and orange patches in Figure 4a respectively). Most of the upper part of the cliff, which collapsed during the 2010 and 2018 destabilization crisis, is constituted of a 100 to 200 meter succession of more recent pyroclastic deposits (Figure 4a, pink patch). The interface with the basal stable layer is marked by a clear slope break, as well as several water seepages (Nachbaur et al., 2019).

The Samperre river has its source at the cliff toe. About 2.5 km downstream, it joins the Prêcheur river (Figure 1). In this upper section, the Samperre river is very narrow (down to 10 m) and steep-walled (the gully is more than 70 m deep at some locations). Slopes reach up to 30° at the cliff bottom (Figure 1b), which favors the remobilization of rock avalanche deposits.

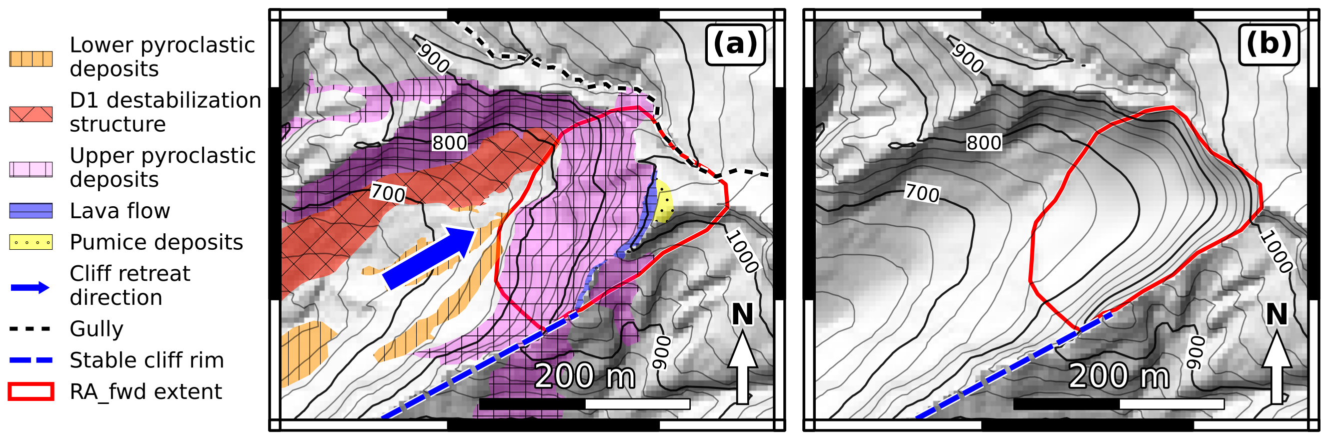

Figure 4. Samperre cliff geology and *RA_fwd* forward prediction scenario. (a) Cliff topography in August 2018 with main geological units (Nachbaur et al., 2019). Vegetation and screes are not displayed. (b) Modified 08/2018 topography with the scar from the potential rock avalanche (*RA_fwd* scenario). The unstable volume is 1.9×10^6 m^3.

Supposedly, the most powerful DFs are thus generated in this part of the river. Further downstream, down to RPRE, average slopes are between 7° and 12°.

In the second section of the river, from the Samperre river / Prêcheur river junction down to the river mouth, the river cuts through relatively poorly resistant materials, such as pumice deposits (Meunier, 1999; Queffféléan, 2018). The river bed progressively widens (from 30 m to 60 or 70 m) and flattens, with 3° to 4° slopes. Thus, it is mainly a deposition area for DFs, with meter-sized blocks scattered over the river bed.

At the mouth of the river, 7 km downstream the Samperre cliff, the Prêcheur village (Figure 2b) is built on the alluvial fan and hosted 1300 inhabitants in 2017 (INSEE, 2020). The bridge (Figure 2b) is the only access to the northern part of the village.

2.2 Topographic surveys and aerial photographs

The main source of quantitative data to constrain initial conditions in simulations are topographic surveys (Table 1 and Table 2). We use three different Digital Elevation Models (DEMs):

- 07/2010 DEM: a 1-m DEM derived from a LiDAR acquisition over the whole river after the main rock avalanches and DFs of 2010. Unfortunately, as the river is rather narrow in its upper section, its quality is rather poor from the cliff bottom down to RPRE.

- 01/2018 DEM: A photogrammetric model of the Samperre cliff was constructed from aerial photographs taken by a drone on Jan. 19, 2018, from which a 1-m DEM of the cliff (which is deprived of vegetation) could be derived.

- 08/2018 DEM: A 1-m DEM derived from a LiDAR acquisition over the whole river. We only modify it slightly at the bottom of the cliff to remove patches of screes, that would otherwise lead to incorrect scree reservoir reconstruction for DF simulation (see Section 3.1.2). This is done in a similar manner to pre-collapse topography and scar reconstruction in (Guimpier et al., 2021). Screes are identified thanks to slope breaks and slope direction variations at the bottom of the cliff, and are then removed by modifying manually the 5 m contour lines of the 08/2018 DEM, using contour lines trends where the cliff is deprived of screes (see Supplementary Figure 1).

Simulations are mainly carried out on the 08/2018 DEM, which has the best quality and is deprived of vegetation. Along with topographic surveys, we also use orthophotographs and aerial photographs taken during helicopter overflights: they help quantifying the cliff evolution in between topographic surveys, as well as the travel distance of rock avalanches and flooded areas after DFs.

2.3 River and cliff monitoring

Since 1975, the occurrence and relative magnitude of collapse events is systematically inferred from the seismic network maintained by the Observatoire Volcanologique et Sismologique de Martinique (OVSM) (Aubaud et al., 2013; OVSM-IPGP, 2020). In this work, we use the broad-band CMG-40T seismic sensor (60 s - 50 Hz), located on the north-eastern side of the Montagne Pelée, about 1.5 km away from the Samperre cliff (LAM station in Figure 1a). Assuming the duration of rock avalanches can be approximated by the duration of seismic signals (Hibert et al., 2011; Levy et al., 2015), seismic recordings give a first insight on the rock avalanche dynamics.

In 1998, 2001 and 2014, three geophones, called Acoustic Flow Monitoring (AFM) sensors (LaHusen, 2005), were installed by the OVSM/IPGP along the river (at CPMA, RPRE and CCPA respectively, see Figure 1a). The AFM system, developed at the Cascades Volcano Observatory (LaHusen, 1998) is the most common system for lahar monitoring, and can be used to trigger alarms. It is currently installed on active volcanoes (e.g. Pinatubo, Marcial et al., 1996, Merapi, Lavigne et al., 2000, Ruapehu, Cole et al., 2009 and Tungurahua, Jones et al., 2015). In this study, we use the so-called FULL channel (signal in 10-300 Hz frequency band, low gain) to estimate the DF travel duration between RPRE and CCPA. Values span between 0 and 4000 mV, but are usually below 50 mV in normal streamflow conditions. In 2010, sampling interval was 10 min and 5 min in normal conditions for CPMA and RPRE respectively, but was reduced to 1 min when the HILO (high gain, low pass) channel exceeded 500 mV at CPMA and 1000 mV at RPRE.

2.4 Granulometry of lahar deposits

11 samples (PR-01 to PR-11) of lahars deposits were recovered for granulometry analysis, at 5 sites along the river, from its outlet to about 5.5 km upstream (Figure 1a). To our knowledge, it is the first time such a sampling campaign is carried out in the Prêcheur river: Meunier (1999) only analyzed the granulometry of streamflow deposits at the river mouth, and Lalubie (2013) similarly recovered one sample only at 80 m altitude (presumably near the CCPA station). More generally, on-site sampling is rarely carried out to constrain numerical simulations. Although they can hardly be used directly to calibrate simulation parameters, they help understand the physical processes controlling flow dynamics.

Granulometric curves as well as an example of a sampling site are presented in Figure 5. All samples contain mainly sand, gravel and boulders, with less than 4% of silts and clays (diameter d<0.1 mm). When compared to granulometric envelopes derived by Bardou et al. (2003) in alpine context, our samples fit neither the "friction-viscous" nor the "viscoplastic" envelopes, whose fine fraction is more important (between 5% and 20% of clay, Figure 5a). Our results are more consistent with grading ranges of lahars deposits on Semeru volcano in Java, Indonesia (Dumaisnil et al., 2010), in particular for hyper-concentrated flow and granular flow deposits (Figure 5b). In their study, granular flows should be understood as DFs with only little silts and clays, such that collision and friction between grains are the main driving forces.

The distinction between DF deposits and HF deposits is not easy as each one can evolve into the other one. Following Dumaisnil et al. (2010) we can associate finer grading (mainly sand and gravel) to HFs (as for sampling sites PR-02, PR-07, PR-11 and PR-10) and coarser, unsorted deposits to DFs (as for sampling sites PR-01 and PR-08).

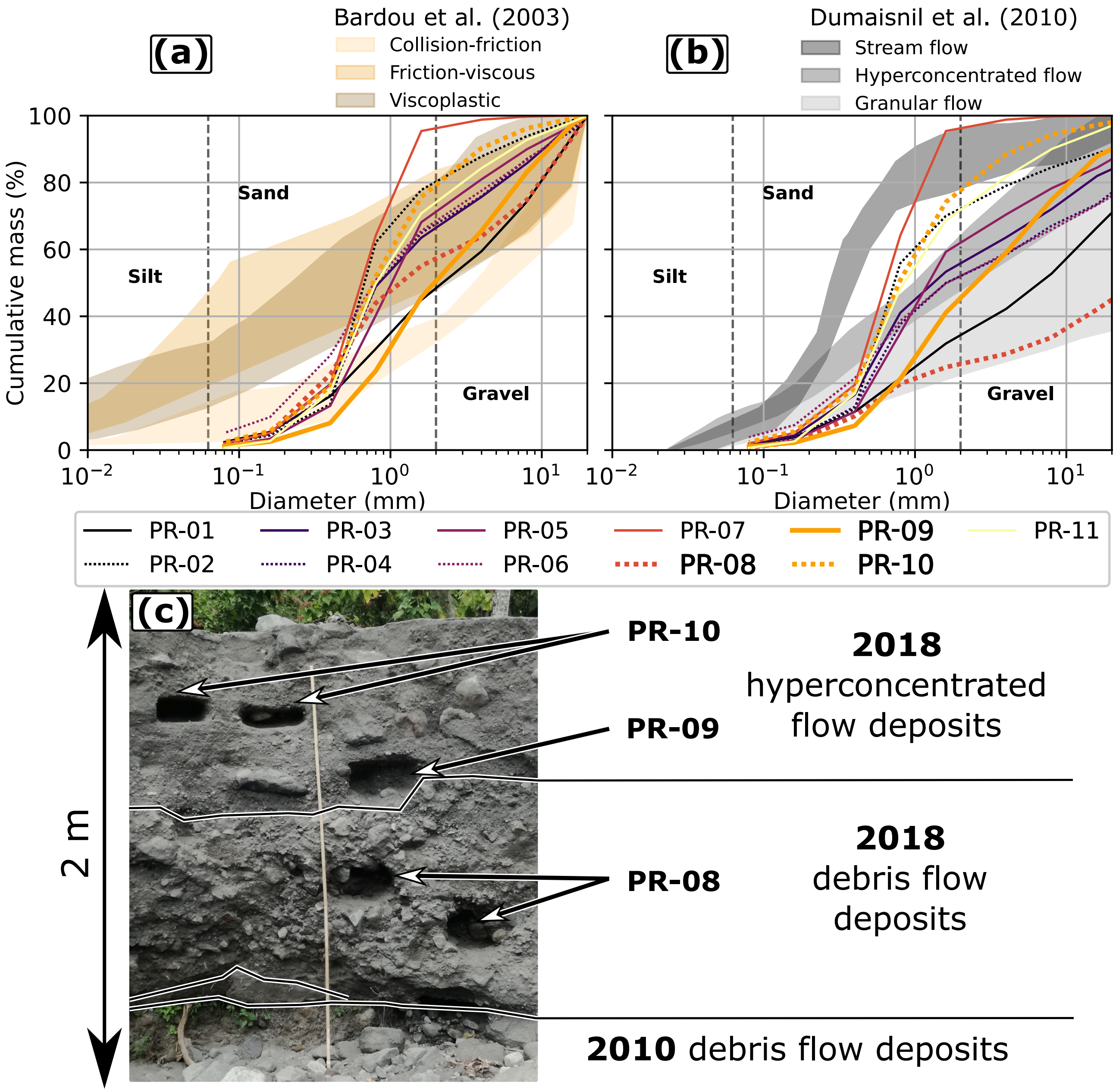

Figure 5. Granulometry of lahar deposits. (a) Lines: granulometry of samples, with boulders larger than 2 cm removed. Colored patches: granulometric envelopes from Bardou et al. (2003) associated to flow rheologies, in alpine context. (b) Lines: granulometry of the whole samples. Grey patches: granulometric envelopes from Dumaisnil et al. (2010), for lahar deposits on the Semeru volcano, Indonesia. (c) Example of sampling site. Granulometric curves of the samples are given in bold in (a) and (b). See Figure 1a for the location of sampling sites (PR-01 is the most upstream sample, and numbering follows stream direction).

3 SIMULATION SCENARIOS FOR CALIBRATION AND FORWARD PREDICTION

We focus on the modeling of extreme events: rock avalanches with volumes above 1×10^6 m^3 and high discharge DFs. In the following we present two such events and explain how we construct the topography and initial volumes for model calibration. This is summarized in the first three columns of Table 2.

3.1 Model calibration: events description and simulation initial conditions

3.1.1 Jan. 4, 2018 rock avalanche

A major episode of destabilization occurred in 2018-2019 on the Samperre cliff. It started on Jan. 2, 2018, after a particularly rainy wet season. Its main phase lasted about two months, but episodic gravitational readjustments occurred until October 2019. This crisis culminated quickly after it started, on Jan. 4, 2018, with one main rock avalanche at 03:00 UTC. It was recorded widely on the seismic network and lasted about 2 minutes (Figure 6). From helicopter overflight, it is estimated to have reached the river bend just upstream RPRE (Figure 1b, green arrow). The 01/2018 DEM gives the geometry of the cliff after the main destabilizations. However, the previous topographic survey, the 07/2010 DEM, is too old to be used as a pre-collapse topography. Indeed, diachronic analysis of ortho-photographs show that the cliff rim retreated by about 50 m between 2010 and 2017 (Nachbaur et al., 2019).

Thus, in order to define the unstable volume involved in the Jan. 4, 2018 destabilization, we use the cliff rim position observed on February 2017 orthophotographs and reconstruct a synthetic cliff topography, as it may have been just before the 2018 destabilization crisis (Figure 3a). This is done by defining a set of longitudinal and transverse cross-sections on the 07/2010 DEM, changing the corresponding profiles with cubic splines, and interpolating the DEM in between, to finally reconstruct the cliff edge as it was in February 2017 (see Supplementary Figure 2).

The post-collapse topography is given by the 01/2018 DEM for the cliff, and by the 08/2018 DEM for the cliff bottom (as deposits of the Jan. 4, 2018 rock avalanche are included in the 01/DEM but had been washed away by August 2018, see Figure 3a). The 1.5×10^6 m^3 unstable volume is then defined as the difference between these two reconstructed topographies. This is our *RA_2018* scenario (Figure 3a, orange patch).

Though the volumes involved in the rock avalanches in 2018-2019 had been the most important since at least 1980, the scree reservoir at the bottom of the cliff was remobilized progressively. Thus, no DF was powerful enough to leave the river bed. In comparison, the DF that occurred on Jun. 19, 2010 flooded the Prêcheur village. In order to have a risk conservative approach and investigate worst-case scenarios, DF modeling will be calibrated on this latter event.

3.1.2 Jun. 19, 2010 debris flow

In May 2010, a series of destabilizations occurred on the Samperre cliff, involving about 2.1×10^6 m^3 (Clouard et al., 2013). After its main phase on May 11, 2010, the first lahar occurred on May, 14 (Aubaud et al., 2013). On Jun. 19, at 7:30 UTM and after a non exceptional tropical wave, a high discharge DF flooded the Abymes quarter in the Prêcheur village.

AFMs records enable the identification of two initial relatively small amplitude surges, with the main phase (that we try to model) occurring between 08:30 and 09:00 UTM (Figure 7a and 7b). The 3000 mV peak value registered at CPMA is particularly high: in all the other lahars from 2009 and 2010, it exceeded 1000 mV on a few occasions only. The signal amplitude then progressively decreased until 11:00 UTM. A last small surge can be spotted at 11:30 UTM, lasting about 30 min (Figure 7a). As pointed out by Aubaud et al. (2013), the triggering rainfall was not particularly strong (11 mm in 1h40), but

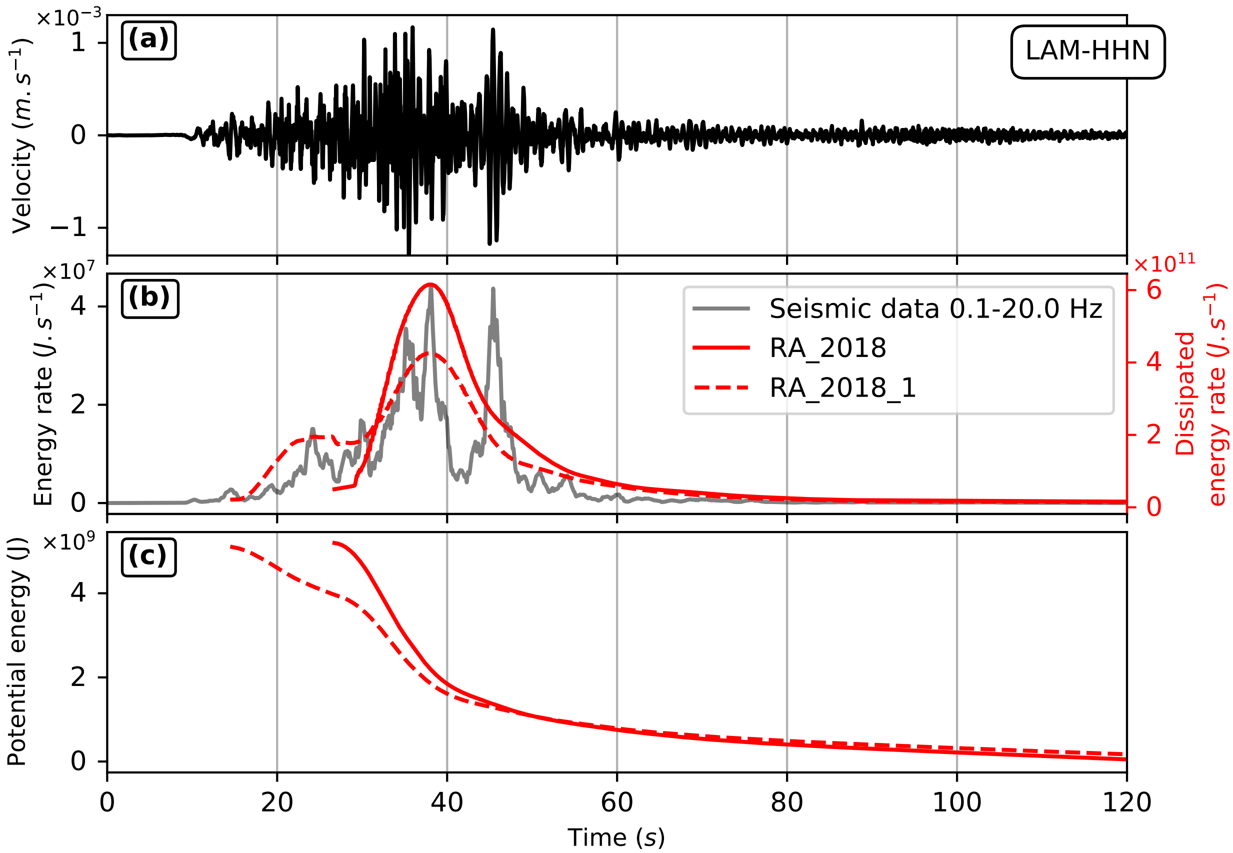

Figure 6. Seismic recordings of the Jan. 4, 2018 Samperre rock avalanche. (a) Signal recorded at station LAM, horizontal northern component. $t = 0$ is 03:00 UTC, Jan. 4, 2018. Signal is filtered between 0.1 and 20 Hz. (b) Grey line: Seismic energy rate at station LAM. Red lines: energy dissipated during the *RA_2018* and *RA_2018_1* scenarios (plain and dashed lines, respectively), with friction coefficient $\mu_S = \tan(14°) = 0.25$. Grey and red lines are aligned for their maximums to match. See Supplementary Note 1 for details on energy computation. (c) Potential energy of the simulated rock avalanche in scenarios *RA_2018* and *RA_2018_1*.

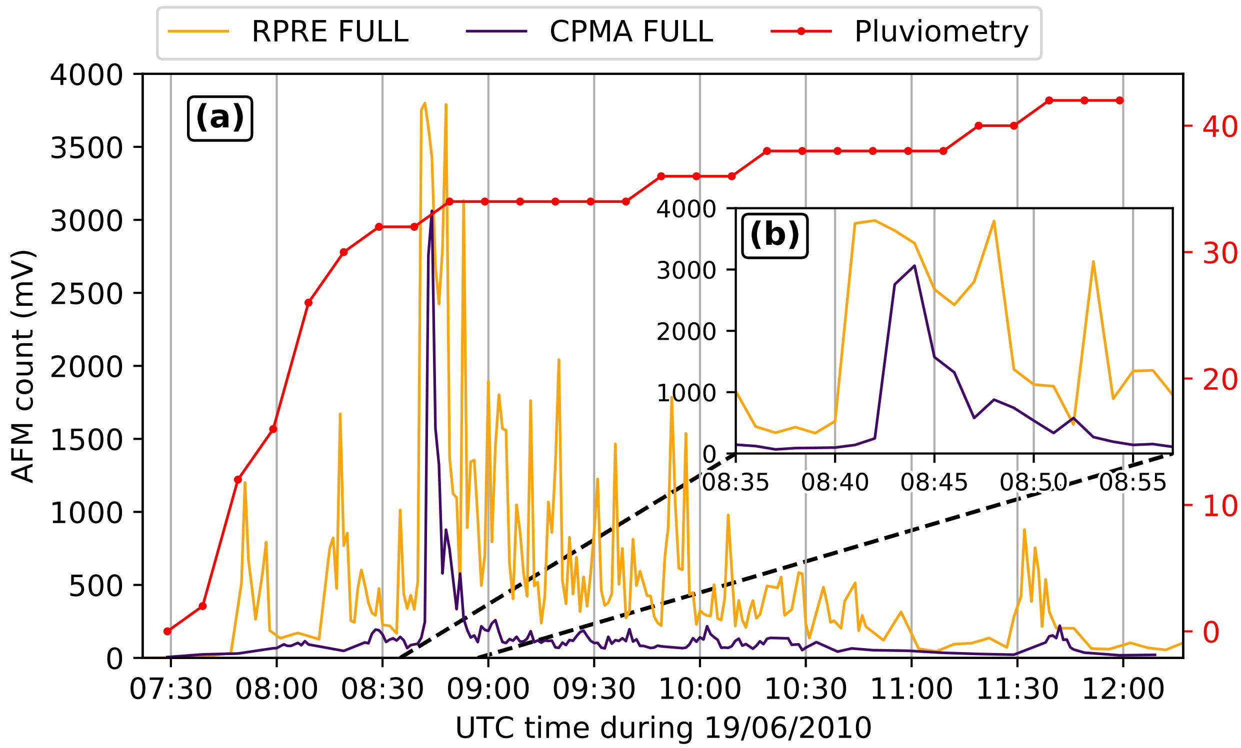

Figure 7. AFMs recordings of the Jun. 19, 2010 lahar from RPRE and CPMA FULL channel. (a) Full event recording, with cumulated pluviometry recorded in CPMA (red line with dots). The black dashed line locates the main event plotted in (b). (b) Main phase of the lahar, with the main DF surge. Time is in hours, UTC.

the main surge was preceded by 1 hour long 30 mm precipitations (as recorded in CPMA station, Figure 7a). This surge was particularly fast: the peak amplitude was recorded with a 2 to 3 min interval between RPRE and CPMA (Figure 7a). Given the 1.5 km distance between the two stations, it yields an average velocity of 30 to 45 km hr^{-1} (8 to 13 m s^{-1}). The extent and location of overflows are given in Figure 1a.

The Jun. 19 2010 lahar is described as a DF by Mathon and Barras (2010) and Laigle and Macabies (2010). The sample PR-06 was recovered from deposits that were not present before the 2010 lahars. As the vegetation cover is too important to have developed after 2018, we associate the sample PR-06 to the deposits of the Jun. 19, 2010 DF. Although it features the highest fine fraction, it remains low and is similar to other deposits: only 5% of clays and silts within the 20 mm fraction, and less than 4% of the total flowing sediment. Even if water circulation may have washed away part of the fine fraction since 2010 (Dumaisnil et al., 2010), what must be actually considered is the clay fraction, which will be even less. Following Coussot and Meunier (1996), we may thus assume that the DF dynamics were controlled by collisional and frictional interactions, and not viscous forces.

The high DF velocity, as well as the screes washout at the cliff toe, suggest it may have been triggered by the instantaneous or at least very quick remobilization of the scree reservoir, in what Lalubie (2013) called a liquefaction triggered lahar. However, no topographic data is available to constrain directly the reservoir. On the contrary, the reservoir produced by the first rock avalanches of the 2018 sequence can be clearly identified on the 01/2018 DEM. Thus, we use the geometry of the 2018 scree reservoir as a proxy for the reservoir remobilized in 2010.

This is done by adjusting a sloping plane on the reservoir surface on the 01/2018 DEM, through a simple Root Mean Square Error (RMSE) minimization between the surface points and a plane, with the CloudCompare software. With a RMSE of 2.1 m, when the reservoir is about 120 m large and 340 m long, the fit is rather good. We assume the 2010 reservoir shared the same characteristics, as the materials involved are similar. The difference between this plane and the 08/2018 DEM provides us with an initial volume of 0.65×10^6 m^3: this is our *DF_2010_1* scenario (Figure 3b, red patch).

As the total volume of the rock avalanches in May 2010 is estimated to 2.1×10^6 m^3 (Clouard et al., 2013), we will also consider a larger reservoir (*DF_2010_2* scenario). This is done by filling the main river bed between the bottom of the cliff and the waterfall (600 m downstream, upper estimation of the maximum distance reached by the rock avalanches in 2010) by a 30 m thick layer of materials (Figure 3b, black hatches). Such a thickness is indeed consistent with observations made during helicopter flights. We thus create a 1.2×10^6 m^3 reservoir.

These simulation scenarios are used to calibrate the model. With the resulting rheological parameters, we will then be able to consider a forward prediction scenario, whose initial conditions are presented in the following section.

3.2 Forward-prediction scenario: simulation initial conditions

In our forward prediction scenario, we model the propagation of a possible future rock avalanche (*RA_fwd* scenario, see Table 2), and the subsequent instantaneous remobilization of the simulated deposits to produce a DF (*DF_fwd* scenario, see Table 2). We use geological and geomorphological data (see Section 2.1) to constrain the initial unstable mass in the cliff. Following its historical retreat direction (Nachbaur et al., 2019), we infer that the north-west part of the cliff is the most likely candidate for future large collapses (Figure 4a and b, red line). Following Nachbaur et al. (2019), the western limit is constrained by the contact between the unstable upper pyroclastic deposits (Figure 4a, pink patch), and the stable basal units (Figure 4a, orange and red patch). We match the northern extent of the unstable volume with the gully running behind the Samperre cliff (Figure 1a, black dashed line). Finally, for the south-east limit, we extend the actual cliff rim towards the north-east: over the past decades, it has constantly progressed in this direction (Figure 1a and 1b, blue dashed line).

Within this extent (Figure 4a and 4b, red line), the topography is modified manually (in the same way as the *2018_1* pre-collapse topography) to get the collapse scar, so that slopes inside and outside the scar are consistent (Figure 4b). The resulting 1.9×10^6 m^3 initial volume of the avalanche is compatible with the volume of previous destabilizations (Clouard et al., 2013; Nachbaur et al., 2019).

The deposits of the simulated rock avalanche will then be instantaneously remobilized to model a subsequent high discharge DF. This is done by changing the rheological parameters in simulations. It will be explained in the next section, where we present the SHALTOP numerical code, that we use to model the propagation of rock avalanches and debris flows.

4 NUMERICAL MODEL

The SHALTOP thin-layer numerical code simulates the dynamics and emplacement of flows on general topographies (Bouchut et al., 2003; Bouchut and Westdickenberg, 2004; Mangeney-Castelnau et al., 2005; Mangeney et al., 2007a). It has been successfully tested to reproduce both real landslide (e.g. Moretti et al., 2015; Brunet et al., 2017; Peruzzetto et al., 2018b) and laboratory experiments (Mangeney-Castelnau et al., 2005; Mangeney et al., 2007a). In SHALTOP, the material layer moving on the topography is considered homogeneous and erosion is not modeled. Energy is dissipated through a force applied at the base of the flow, in the opposite direction to flow velocity. We use the same rheological law in the whole DF, without considering

Table 2. Simulation scenarios for model calibration and forward prediction

	RA_2018	*DF_2010_1*	*DF_2010_2*	*RA_fwd*	*DF_fwd*
Purpose	Calibration for rock avalanche (Jan. 4, 2018 rock avalanche)	Calibration for debris flow (Jun. 19, 2010 debris flow)		Forward prediction simulation (rock avalanche)	Forward prediction simulation (debris flow)
Bed topography	01/2018 in the cliff sector, 08/2018 DEM elsewhere (modified manually to remove deposits)	08/2018 DEM (modified manually to remove deposits)		08/2018 DEM (modified manually to construct collapse scar)	08/2018 DEM (modified manually to remove deposits)
Initial volume geometry	Difference between 2017 DEM (reconstructed) and 01/2018 DEM	Difference between 01/2018 and 08/2018 DEMs	Difference between 01/2018 and 08/2018 DEMs + 30 m of materials over 600 m downstream	Difference between 08/2018 DEM and synthetic collapse scar	Deposits of the *RA_fwd* rock avalanche simulation
Volume ($\times$**10^6 m^3**)	1.5	0.65	1.2	1.9	1.9
Calibrated rheological parameters	$\mu_S = \tan(14°)$	Coulomb: $\mu_S = \tan(2°)$ or $\mu_S = \tan(3°)$ Voellmy: $\mu_S = \tan(2°)$ and $\xi = 500$ m s^{-2}			

possible dilution and sediment settling at its tail.

We model rock avalanches with the Coulomb rheology, as it proved to reproduce correctly real landslides deposits (e.g. Lucas and Mangeney, 2007; Lucas et al., 2014; Peruzzetto et al., 2019) and dynamics when compared to the force inverted from seismic data (Favreau et al., 2010; Yamada et al., 2018; Moretti et al., 2020). With this rheology, the basal stress T is:

$$T = \mu_S \rho h (g \cos(\theta) + \gamma u^2), \tag{1}$$

where $\mu_S = \tan(\delta)$ is the friction coefficient and δ the friction angle, ρ is the flow density, h the flow thickness, g the gravity field, θ the local slope angle, γ the topography curvature along flow path and u the velocity norm. Note that in SHALTOP, γ is computed with the topography curvature tensor (see Peruzzetto et al. (2021) for details). In Equation (1), μ_S is used to take into account empirically all dissipative processes occuring within the flow. Other more complex rheologies exist to describe internal friction, e.g. with a soil mechanics approach (Savage and Hutter, 1989), or the $\mu(I)$-rheology (GDR MiDi, 2004; Jop et al., 2006). Nevertheless, these modeling solutions are either still debated (Gray et al., 2003), or only adapted to flow on simple topographies (e.g., inclined planes in Baker et al., 2016). With the Coulomb rheology, the friction coefficient μ_S needed to model observed deposits decreases as the volume of the avalanche increases (Lucas et al., 2014), at least for dry avalanches. Lucas et al. (2014) suggest the empirical relation between μ_S and the landslide volume V:

$$\mu_S = V^{-0.0774} \tag{2}$$

Such friction coefficients also proved to reproduce correctly the dynamics of both large (Moretti et al., 2015; Yamada et al., 2018) and small (Levy et al., 2015) landslides. Using this relation with our 1.5×10^6 m^3 volume estimation of the Jan. 4, 2018 rock avalanche, we get $\mu_S = \tan(18.4°) = 0.33$. However, as shown for instance in Peruzzetto et al. (2019), this estimation may sometimes underestimate the mobility of the rock avalanche, especially when water is present in the avalanche. To model such water-laden avalanches, it is necessary to decrease the friction coefficient μ_s in simulations. Thus, for model calibration, we test friction coefficients between $\mu_S = \tan(10°) = 0.18$ and $\mu_S = \tan(20°) = 0.36$.

In order to model the DF, we use frictional rheologies and do not consider visco-plastic rheologies (e.g. Pastor et al., 2004), as suggested by the granulometry of deposits (see Section 2.4). We test the Coulomb rheology with a friction coefficient lower than for rock avalanche simulation: their simulated deposits can thus be remobilized. We use $\mu_S = \tan(2°) = 0.03$ and $\mu_S = \tan(3°) = 0.05$. Such values are low in comparison to other DF simulations carried out with SHALTOP (e.g., $\mu_S = \tan(8°)$ in Moretti et al., 2015). However, with $\mu_S \geq \tan(4°)$, the flow would stop before it reaches the Prêcheur village, which is not consistent with observations of the Jun. 19, 2010 DF. Besides, such low values are not uncommon in the literature to model lahars on volcanic slopes (e.g. Pastor et al., 2018a; Frimberger et al., 2021).

For snow avalanche and debris flow modeling, the empirical Voellmy rheology is also commonly used (Salm, 1993; Hungr et al., 2007; Pastor et al., 2018a). It introduces in the basal stress a turbulence term proportional to the square velocity:

$$T = \mu_S \rho h (g \cos(\theta) + \gamma u^2) + \rho g \frac{u^2}{\xi}, \tag{3}$$

Following Zimmermann et al. (2020), we choose turbulence coefficients ξ between 100 m s^{-2} and 500 m s^{-2}. Influence of further increasing ξ is investigated with the Coulomb rheology, as it is equivalent to choosing infinite values for ξ.

5 CALIBRATION AND FORWARD PREDICTION SIMULATION RESULTS

5.1 Rock avalanche back-analysis

The travel distance of the *RA_2018* rock avalanche scenario with various friction coefficients is displayed in Figure 8. The extent of the Jan. 4, 2018 deposits (dashed green line in Figure 8) is best reproduced with $\mu_S = \tan(14°) = 0.25$. This is less than $\mu_S = \tan(18.4°) = 0.33$, that is derived from the empirical law of Lucas et al. (2014) (see Section 7.1.1 for further discussion). With $\mu_S = \tan(14°)$, the flow dissipated energy rate reproduces correctly the main seismic energy increase phase (Figure 6b, at 30 s). The durations of the sismic signal (60 s) and of the main phase of the simulated energy dissipation (80 s) are also similar (see Supplementary Note 1 for details on energy computation). However, the flow dissipated energy rate fails to reproduce the signal complexity, with successive energy peaks (see Section 7.1.2 for a discussion). While most of the energy is dissipated after 100 s (Figure 6b, red plain line), at that time the flow front is still mobile, about 500 m away from its final position (see Supplementary Figures 3 and 4). Afterwards, 600 s are still needed for the front to stop. This behavior will be discussed later on (see Section 7.1.2).

For the forward prediction DF simulation, we use the deposits of the rock avalanche simulation as the initial reservoir. Considering that the extent of deposits observed in 2018 is well reproduced with $\mu_S = \tan(14°)$, we use this parameter to model a potential future rock avalanche, even though the dynamics of the rock avalanche may not be properly modeled.

5.2 Debris flow back-analysis

In the *DF_2010_1* scenario, the Voellmy rheology with $\mu_S = \tan(2°)$ and $\xi = 500$ m s^{-2}, and the Coulomb rheology with $\mu_S = \tan(2°)$ and $\mu_S = \tan(3°)$, reproduce relatively well observed flooded areas as well as travel durations.

In the village, the thickness of the deposits is mostly below 1 m (Figure 9a-e). On the right bank, the best fit with observations is obtained with Coulomb and $\mu_S = \tan(2°)$ (Figure 9c). On the left bank, other 2010 overflows are reproduced by all simulations (Figure 9a-c, green outlines between the bridge and CCPA). However, the flooded area on the left bank is over-estimated, especially with $\mu_S = \tan(2°)$ (both with the Coulomb and the Voellmy rheologies, Figure 9d).

The Jun. 19, 2010 DF travel duration between RPRE and CPMA (1.5 km) is estimated from AFMs recordings between 1 and 4 min. When picking the maximum discharge time at these locations in simulations, only the Coulomb rheology with

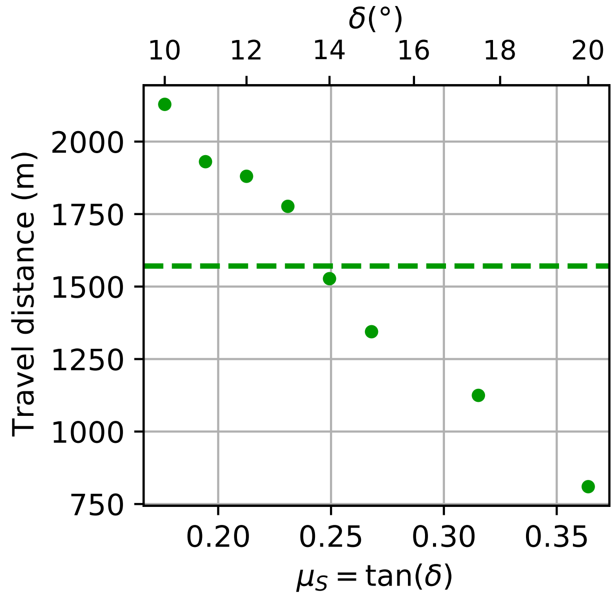

Figure 8. Simulation results for *RA_2018* rock avalanche simulations, with various friction coefficients $\mu_S = \tan(\delta)$. Travel distances are measured from the cliff toe (white cross in Figure 1b and 3b). Error bars (computed by considering 1 to 10 m thickness thresholds when locating the extent of the deposits) are not displayed, but are at most twice the size of the markers. The green dashed line is the observed travel distance of the Jan. 4, 2018 rock avalanche.

$\mu_S = \tan(2°)$ could reproduce a 4 min interval (Figure 9f, blue plain line). The second and third smallest interval are 5 min (Voellmy, $\mu_S = \tan(2°)$ and $\xi = 500$ m ^{2}) and 5 min 20 s (Coulomb, $\mu_S = \tan(3°)$). For these 3 simulations, the corresponding flow durations between RPRE and the Prêcheur bridge (4,3 km) vary between 10 and 24 min (Figure 9g).

In comparison, the *DF_2010_2* scenario, that involves a larger volume (1.2×10^6 m^3), yields travel durations that are more compatible with observations, both with Coulomb and $\mu_S = \tan(2°)$ or $\mu_S = \tan(3°)$, and with Voellmy and $\mu_S = \tan(2°)$ and $\xi = 500$ m s^{-2} (Figure 10f). With these parameters, the flow travel time between RPRE and the bridge is less than 20 min (Figure 10g). However, flooded areas are largely over-estimated, both on the right and left banks (Figure 10a-d). In particular with Coulomb and $\mu_S = \tan(2°)$, the DF runs over the river right bank about 400 m downstream CCPA, and enters two adjacent gullies (Figure 10c, black dashed lines on the northern side of the river). This suggests scenario *DF_2010_1* is more realistic than scenario *DF_2010_2* to reproduce the Jun. 19, 2010 DF.

Considering the uncertainty on the calibration parameters for DF simulation, we use Coulomb (with $\mu_S = \tan(2°)$ or $\mu_S = \tan(3°)$) and Voellmy (with $\mu_S = \tan(2°)$ and $\xi = 500$ m s^{-2}) for DF modeling in the forward prediction simulation.

5.3 Forward-prediction simulation results

In the *RA_fwd* scenario, we model a potential future 1.9×10^6 m^3 rock avalanche from the Samperre cliff with Coulomb and the calibrated friction coefficient $\mu_S = \tan(14°) = 0.25$. The final deposits are similar to the *RA_2018* simulation (1.5×10^6 m^3) with the same friction coefficient, as they extend only a few tens of meters further downstream (Figure 11a). Their maximum thickness is about 30 m.

This reservoir is then used as a source term for the propagation of the DF. Following the calibration results, we test three rheologies: the Voellmy rheology with $\mu_S = \tan(2°)$ and $\xi = 500$ m s^{-2}, and the Coulomb rheology with $\mu_S = \tan(2°)$ or

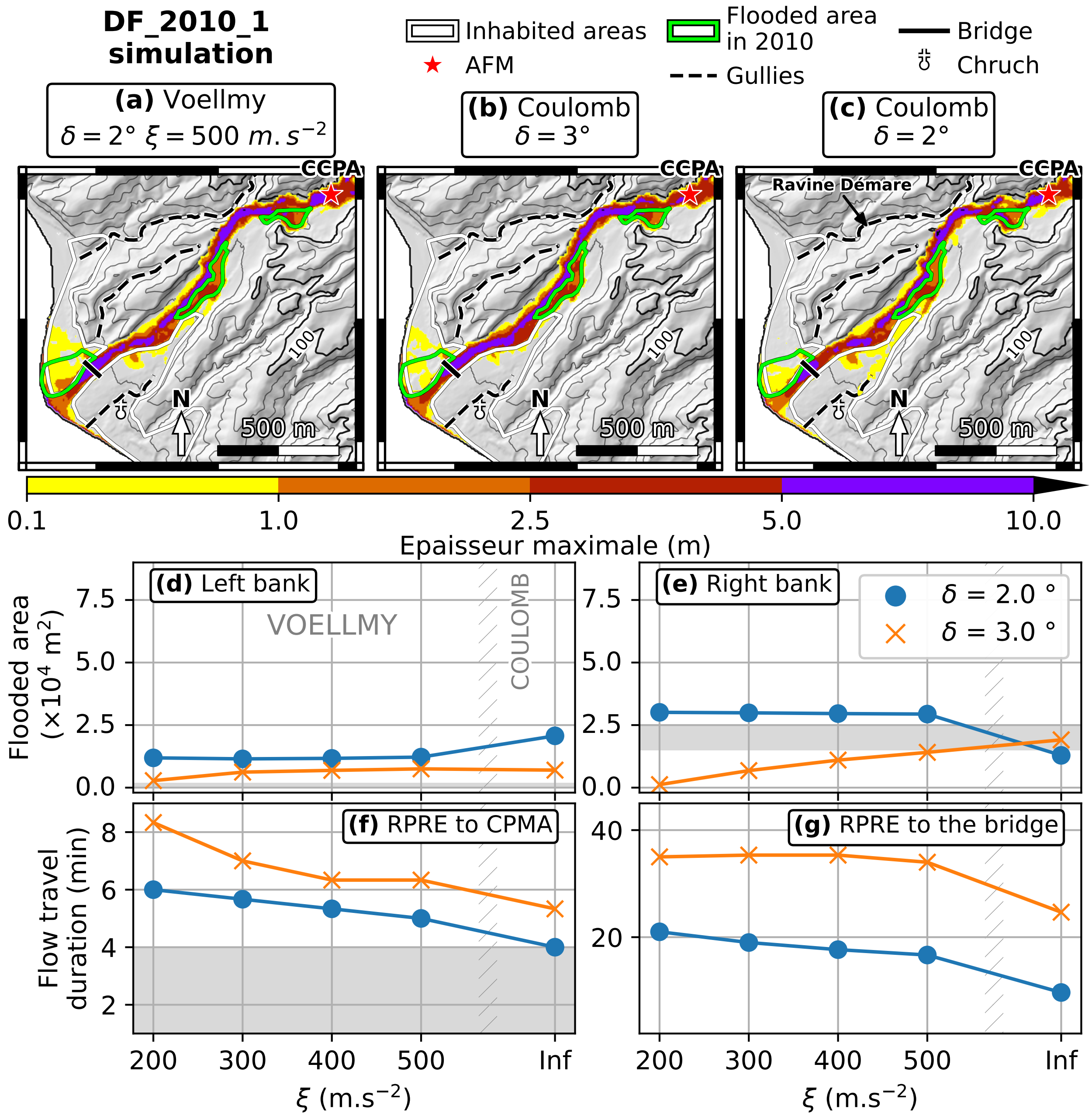

Figure 9. Simulation results for the *DF_2010_1* scenario (0.65×10^6 m^3). (a) Maximum flow thickness with the Voellmy rheology, $\mu_S = \tan(2°) = 0.03$ and $\xi = 500$ m s^{-2}, (b) with the Coulomb rheology and $\mu_S = \tan(3°) = 0.05$, and (c) with the Coulomb rheology and $\mu_S = \tan(2°) = 0.03$. Topography is the 08/2018 DEM. Each point in (d), (e), (f) and (g) is a simulation result, with friction coefficient given by line color and turbulence coefficients given by the x-coordinate. Left of hatches is for the Voellmy rheolgy, right is for the Coulomb rheology (equivalent to infinite turbulence coefficient). (d) and (e): Area flooded on the left (d) and right (e) riverbank, within inhabited areas. (f) and (g): Flow travel duration between RPRE and CPMA ((f), about 1.6 km), and between RPRE and the Prêcheur bridge ((g), about 4.3 km), measured by picking the maximum of the discharge at each location. Grey patches are observations for the Jun. 19, 2010 DF, taking into account uncertainties.

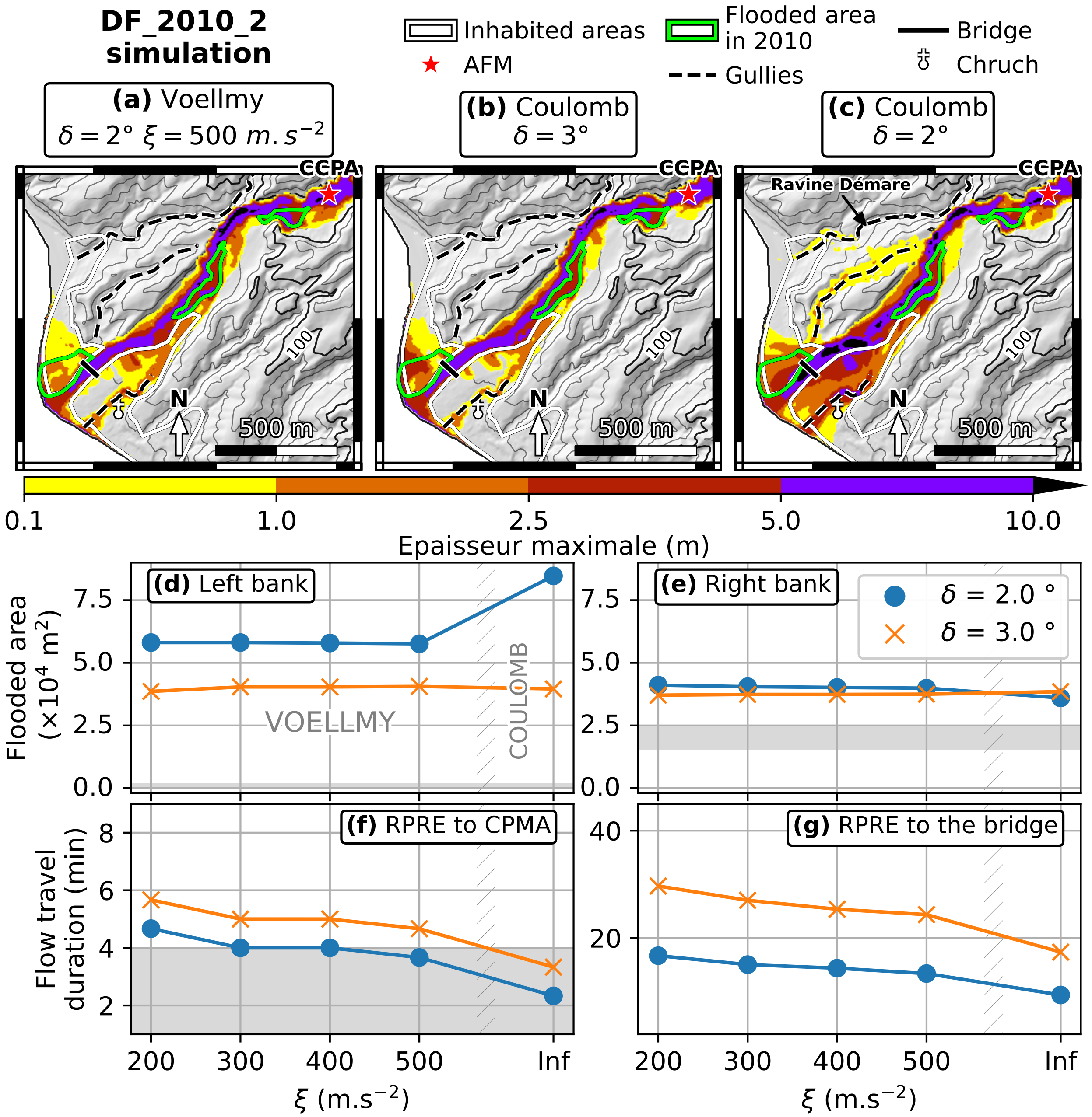

Figure 10. Simulation results for the *DF_2010_2* scenario (1.2×10^6 m^3). See Figure 9 for legend.

$\mu_S = \tan(3°)$. With the Voellmy rheology,travel durations and flooded areas are very similar to results derived in the *DF_2010_2* scenario (Supplementary Figure 5). However, the DF velocity is reduced by about 10% when the Coulomb rheology is used. As a matter of fact, in comparison to the *DF_2010_2* scenario, the initial mass is spread more broadly in the river bed, such that the flow front accelerates on a shorter distance. This effect is not observed with Voellmy because the turbulent term in Equation (3) prevents the flow from accelerating indefinitely. Peak discharges at RPRE vary between 4,000 and 6,000 m^3 s^{-1} (Figure 11b-d, blue lines): this is coherent with field observations in other contexts, for this range of volumes (see Figure 2 in Rickenmann, 1999). With Coulomb and $\mu_S = \tan(3°)$, some of the flowing material stops before it reaches the sea, such that the peak discharge at the bridge does not exceed 400 m^3 s^{-1}. To the the contrary, $\mu_S = \tan(2°)$ increases mobility, and peak discharges reach almost 1000 m^3 s^{-1} with the Voellmy rheology (Figure 11c), and more than 1600 m^3 s^{-1} with the Coulomb rheology (before the DF overflows the river bed, Figure 11d).

These results provide a first insight on the most exposed areas in the case of a future massive rock avalanche followed by a high discharge DF remobilizing all deposits, provided the rock avalanche and DF have similar behaviours and solid content as the events used for calibration. In the following, we investigate the influence of initiation processes and location on the simulation results.

6 SENSITIVITY ANALYSIS: INFLUENCE OF INITIATION MECHANISM

6.1 Influence of successive destabilizations on rock avalanches simulations

To investigate the influence of retrogressive destabilizations on runout prediction, we release the 1.5×10^6 m^3 of the *RA_2018* in two successive steps, instead of one. In the resulting *RA_2018_2* scenario, 0.8×10^6 m^3 are first released at the cliff bottom (A in Supplementary Figure 6a), and the rest (B in Supplementary Figure 6a) collapses 13 s later. The two volumes are constructed arbitrarily by separating the extent of the initial mass of the *RA_2018* scenario approximately at the middle of the cliff. Thus, the resulting two volumes are similar.The 13 s delay between the two collapses matches the initial duration of the seismic signal before the seismic energy starts increasing sharply (see Figure 6b). Because SHALTOP models one-phase/one-layer flows, it should be noted that in the *RA_2018_2* scenario, the second avalanche is assumed to be mixed with the first one as soon as they join. As a result, we do not model the possible development of a two-layer flow, with the second avalanche propagating above the first one. This could enhance mobility by flattening the topography and favoring erosion (Mangeney et al., 2010; Farin et al., 2014).

Successive collapses do help reproduce, to some extent at least, the complexity observed in the Jan. 4, 2018 seismic signal (compare red dashed line and black line in Figure 6b). However, the geometry of final deposits (and thus the geometry of the debris reservoir that will be remobilized later on as a DF) remains the same (compare Supplementary Figure 6b and 6d).

6.2 Influence of progressive release on debris flows simulations

In our DF simulations, the initial reservoir is remobilized instantaneously. Although we manage to reproduce rather correctly the flooded area and travel times of the Jun. 19, 2010 DF, it is in general difficult to characterize the initiation process of DFs. Besides, for a given debris reservoir, the initiation mechanism may not be independent from the remobilized volume. Such correlations are beyond the scope of this study. In this section, we only explore the influence of the initiation process on debris flow dynamics, for a given debris flow volume. In order to investigate empirically the effect of progressive remobilization, we release 0.65×10^6 m^3 (i.e., the same volume as in the *DF_2010_1* scenario) over a 200 m^2 area at the cliff bottom (white cross

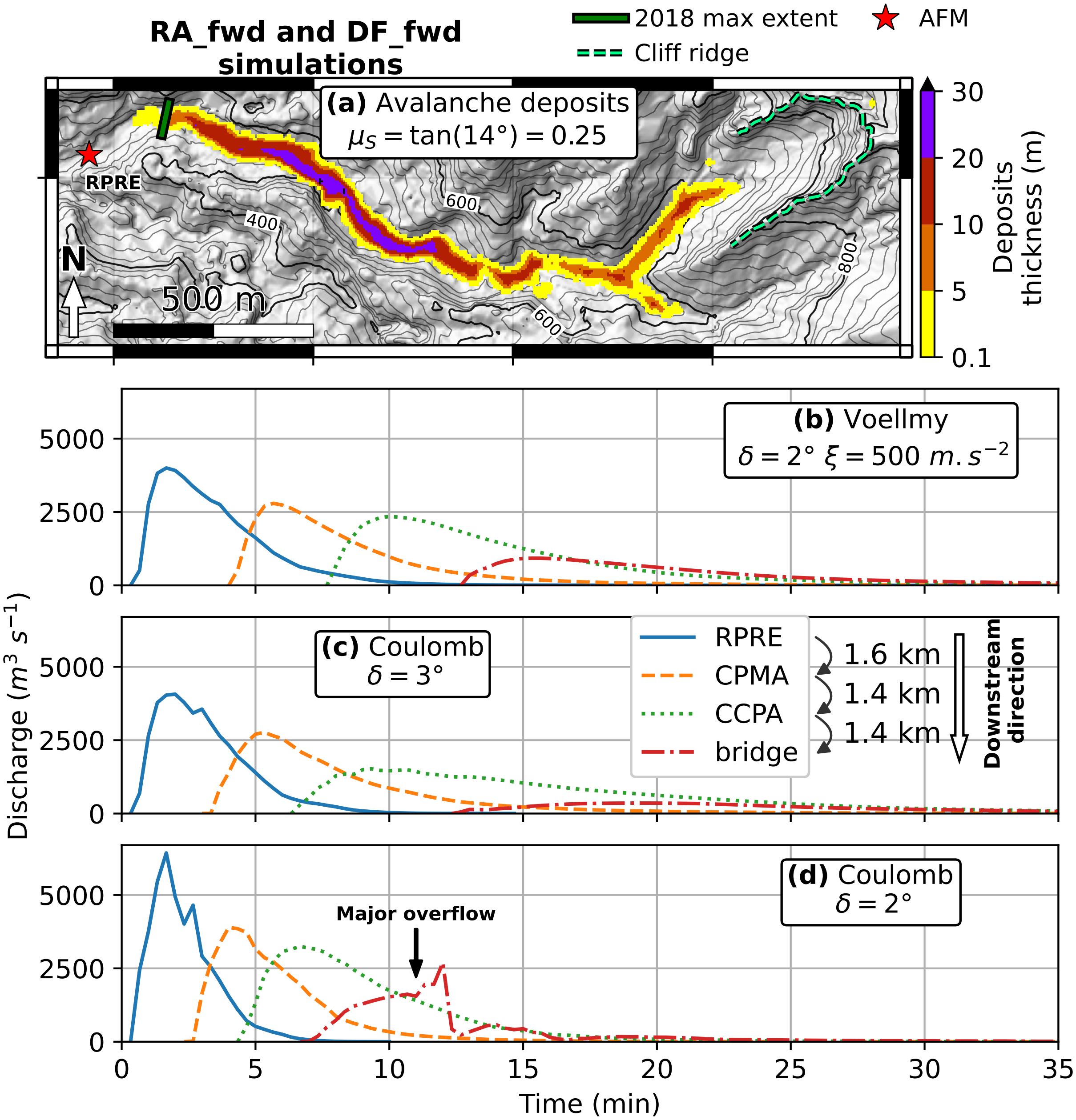

Figure 11. Results of the *RA_fwd* rock avalanche scenario and subsequent *DF_fwd* DF simulation. (a) Final deposits of the rock avalanche, modeled with Coulomb and $\mu_S = \tan(14°) = 0.25$. The green line is the observed runout of the Jan. 4, 2018 rock avalanche. The topography is the 08/2018 DEM. (b), (c) and (d): Simulated discharges at RPRE, CPMA, CCPA and the bridge. (b) Voellmy rheology, $\mu_S = \tan(2°)$ and $\xi = 500$ m s^{-2}. (c) Coulomb rheology, $\mu_S = \tan(3°)$. (d) Coulomb rheology, $\mu_S = \tan(2°)$. Strong variations in (d) for discharge at the bridge result from major overflows around the bridge (see Supplementary Figure 5c).

in Figure 3), through a constant discharge lasting $\Delta t = 10$ or 20 min. Thus, simulations differ solely by the release duration, allowing for the comparison of results. The initial discharge is thus inversely propotionnal to Δt. Results are given in Figure 12. Increasing release duration slows down the DF and reduces flooded area. Using $\Delta t = 10$ min and the Coulomb rheology with $\mu = \tan(2°)$ enhances the match between observed and simulated flooded areas, but over-estimates slighlty the travel duration between RPRE and CPMA (compare blue circles and shaded area in Figure 12d-f). Note that in Figure 12 travel durations are measured by picking the onset of discharge increase, because no clear maximum can be identified in RPRE when we impose a constant discharge in the source area (see Figure 13b).

If we assume AFM records are qualitative proxys for flow discharge at nearby locations, the temporal evolution of RPRE's record (with a sharp increase and a progressive decrease) of the Jun. 19, 2010 DF is better reproduced with an instantaneous release (compare Figures 13a and 13c). However, the 15 min duration of the flow at RPRE is better reproduced with a progressive release (compare Figures 13b and 13c). This may indicate that most of the debris involved in the Jun. 19, 2010 DF was released instantaneously, but that part of the initial reservoir was remobilized afterwards. Thus, more realistic initial set-up would involve a non constant discharge, but such initial conditions are not implemented in SHALTOP. Nevertheless, an instantaneous release proved to be sufficient to reproduce the main characteristics of the Jun. 19, 2010 DF (travel duration and flooded area), at least in a first approximation.

6.3 Influence of source area on debris flow simulations

For a given released volume, the location of the release area has in comparison little influence on the results of DF simulations. When the release is instantaneous, we saw that the *DF_2010_2* and *DF_fwd* scenarios, that involve similar volumes but different initial geometries, yield similar results (see Figure 10 and Supplementary Figure 5). The same conclusion is drawn when using a constant discharge, located either at the cliff bottom, at the waterfall or at RPRE (see Figure 1 for locations): travel durations and flooded areas are very similar (see Supplementary Figure 7).

7 DISCUSSION

7.1 Rock avalanche modeling

7.1.1 Choice of rheological parameters

In this study, the friction coefficient μ_S used in the rock avalanche forward prediction simulation is chosen after a calibration step, as often done in the literature (e.g. Sosio et al., 2012; Pastor et al., 2018a). To our knowledge, it is difficult to estimate μ_S directly from physical characteristics of the materials. Indeed, simulations of laboratory experiments involve high friction coefficient (for instance, $\mu_S = \tan(30°)$ in Gray et al., 1999) that fail to reproduce deposits and dynamics observed at the field scale.

If no calibration data are available, another solution is to use empirical laws derived from field observations. Lucas et al. (2014) estimate the mobility of landslides through the effective friction coefficient μ_{eff}. μ_{eff} differs from the traditional angle of reach (or Heim's ration) μ_H: while μ_H only depends on the landslide runout, μ_{eff} also takes the initial mass geometry into account. We have:

$$\mu_{eff} = \tan(\theta) + \frac{H_0}{\Delta L}, \tag{4}$$

$$\mu_H = \frac{H}{\Delta L'}, \tag{5}$$

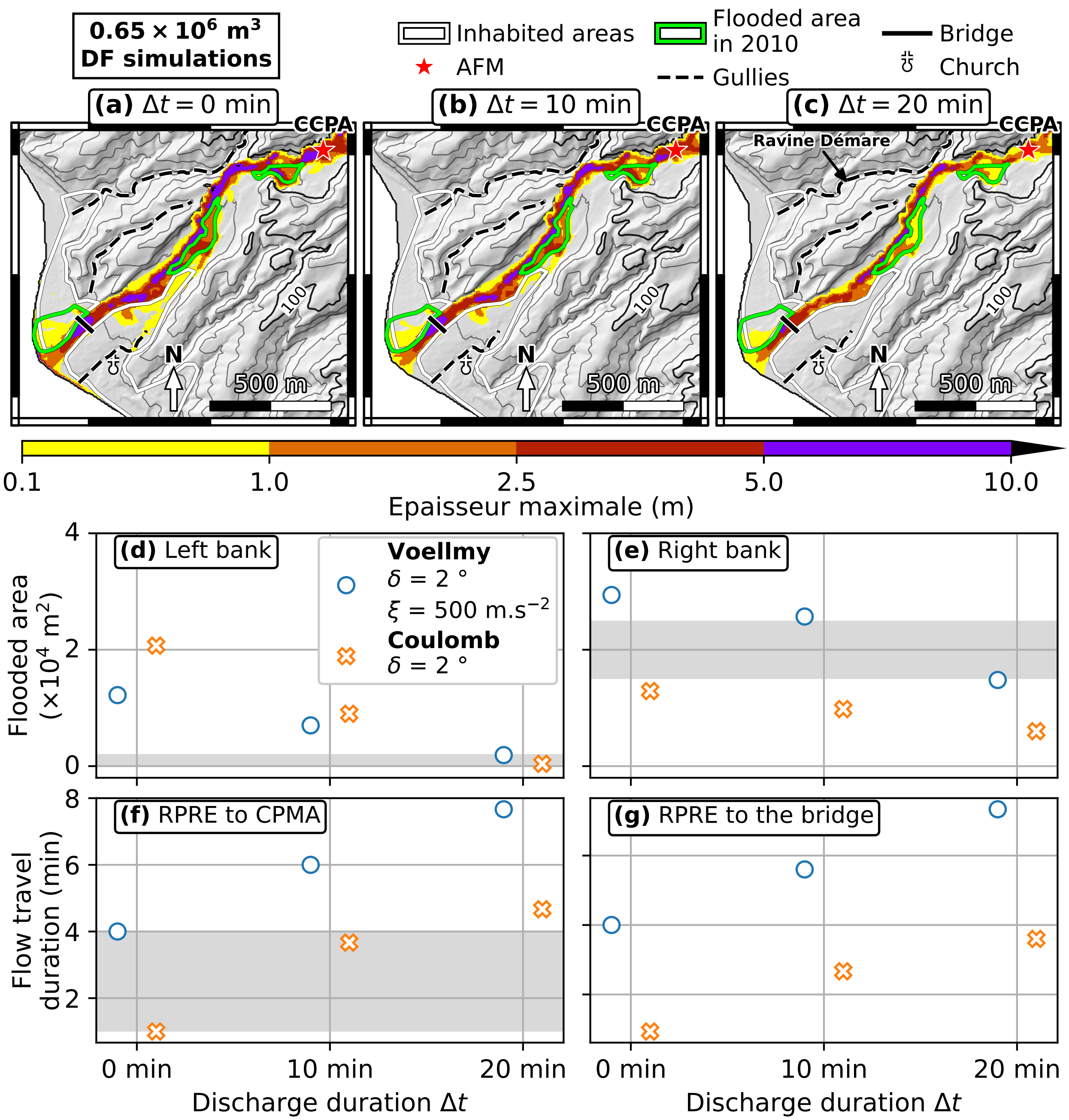

Figure 12. *DF_2010_1* simulation with instantaneous or progressive release (10 or 20 min, see abscissa). The released volume is always 0.65×10^6 m^3. (a), (b), (c) Maximum flow thickness, for different durations Δt of initial discharge.(d) and (e): Area flooded on the left (d) and right (e) riverbank, within inhabited areas. (f) and (g): Flow travel duration between RPRE and CPMA ((f), about 1.6 km), and between RPRE and the Prêcheur bridge ((g), about 4.3 km), measured by peaking the onset of discharge increase. Grey patches are observations for the Jun. 19, 2010 DF, taking into account uncertainties.

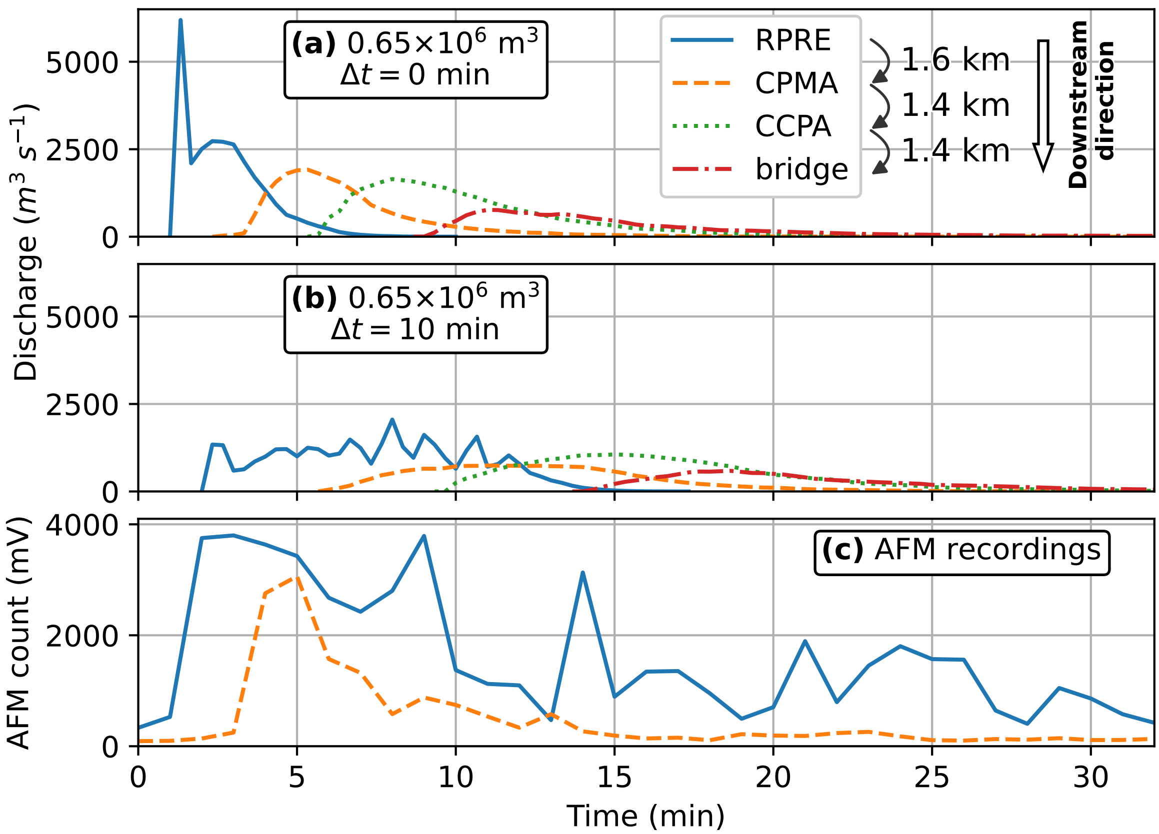

Figure 13. Comparison between simulated discharges at fixed locations and AFMs recordings. (a) Simulated discharges at RPRE, CPMA, CCPA and at the bridge (see Figure 1 in the main body of the article for locations) for the *DF_2010* scenario, with Coulomb and $\mu_S = \tan(2°)$, and an instantaneous release. (b) Same as (a), but with a constant source discharge during 10 min. (c) AFM recordings at RPRE and CPMA for the Jun. 19, 2010 DF. $t = 0$ min is 8:39 UTC, Jun. 19, 2010.

with θ the topography average slope along flow path, H_0 the maximum thickness of the initial mass and ΔL the landslide travel distance along topography from the scar toe. H (drop height) and $\Delta L'$ are respectively the difference in altitude and horizontal distance between the upper scar and furthest deposits location (see supplementary materials in Lucas et al., 2014). The expression (4) of μ_{eff} is derived from the analytical solution of thin-layer dam-break (Mangeney et al., 2000; Faccanoni and Mangeney, 2012). Lucas et al. (2014) use a database of terrestrial and non-terrestrial landslides with a small amount of water to estimate empirical relations relating μ_H and μ_{eff} to the landslide volume V:

$$\mu_{eff} = V^{-0.0774}, \tag{6}$$

$$\mu_H = 1.2V^{-0.089}. \tag{7}$$

When we apply these relations to the 2018 Samperre rock avalanches, we get values between $\tan(18.5°) = 0.33$ and $\tan(19.5°) = 0.35$ for both μ_H and μ_{eff}. This is in good agreement with values computed directly from observations, using Equations (4) and (5) (between $= \tan(19°) = 0.34$ and $= \tan(19.5°) = 0.35$ for both μ_H and μ_{eff}).

In comparison, we used $\mu_S = \tan(14°) = 0.25$ to reproduce observed travel distances. It has been shown that μ_H cannot be used to estimate directly the flow mobility: although it is related to the effective mobility of the landslide, it also includes purely geometrical descriptors such as topographic slope or initial mass geometry (e.g. Lucas and Mangeney, 2007; Lucas et al., 2014). The latter are corrected add by the more complex definition of μ_{eff}, such that it proved to better estimate the friction coefficient μ_S needed to reproduce real landslides (Lucas et al., 2014). As shown in Figure 14, the empirical relation (6) is globally in agreement with values of μ_S calibrated with SHALTOP on other sites. Nevertheless, significant dispersion is observed both for the empirical relation (see the 95% confidence interval for Equation (6), shaded area in Figure 14) and calibrated values (e.g., for volumes above 10^8 m^3, Figure 14). This dispersion may be partly explained by the fact that μ_S does not depend only on volume. The mobility also depends, for instance, on water content (e.g. Peruzzetto et al., 2019), path material (Aaron and McDougall, 2019) and erosion processes (Mangeney et al., 2010). Besides, the expression of μ_{eff} was derived for flows on constant and laterally uniform slopes. The generalization of Equation (4) to general topographies with, for instance, varying slopes and bended channels is not straightforward. This may also explain the uncertainty of the empirical relation (6), and the difference with calibrated values of μ_S.

Interestingly, Equation (6) seems to over-estimate μ_S when calibration is done by reproducing deposits (blue circles and white square in Figure 14), and slightly under-estimate μ_S when calibration uses seismic signal (pink crosses and orange diamond in Figure 14). This is consistent with results of Moretti et al. (2020): when they use only the force applied on the ground (inverted from seismic recordings) to calibrate μ_S, the observed travel distance is under-estimated. However, Lucas et al. (2014) do not highlight any systematic bias between μ_{eff} and values of μ_S calibrated from deposits (see their Figure 3b). To investigate more thoroughly these discrepancies, a larger database of back-analyzed landslides would be needed. This is beyond the scope of this study, but highlights the uncertainty associated to the calibration of simulation parameters.

7.1.2 Influence of initiation mechanism on deposits geometry

The fact that for a given volume, the initiation mechanism has little influence on the travel distance is consistent with results from Moretti et al. (2015) who model the 2010 Mount Meager landslide, with 1, 2 or 3 successive collapses. It can can be explained by the fact that the initial potential energy is dissipated quickly in the first 30 s to 50 s (see Figure 6c). Indeed, whatever the initiation mechanism, the rock avalanche is blocked at the inlet of the Samperre river (just upstream the waterfall, see Figure 1), that is too narrow for the avalanche to enter it at once. Then, the rock avalanche can move further downstream

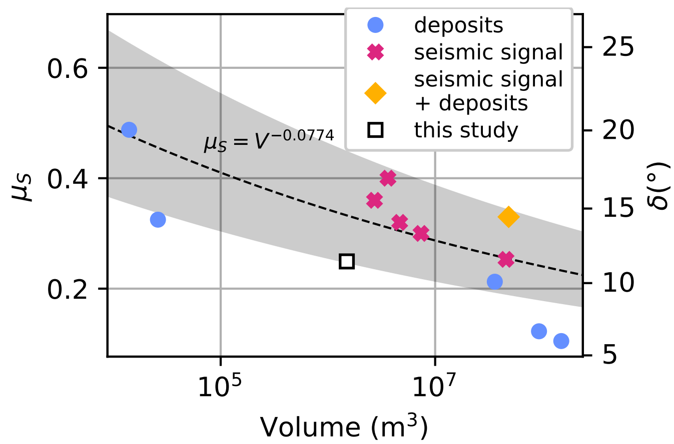

Figure 14. Values of $\mu_S = \tan(\delta)$ calibrated with SHALTOP to reproduce terrestrial landslides with a single constant friction coefficient, using deposits and/or seismic data (Lucas et al., 2007; Kuo et al., 2009; Moretti et al., 2015, 2020; Yamada et al., 2018; Peruzzetto et al., 2019). See Supplementary Table 1 for details. The square is the calibration result of the *RA_2018* simulation. The black dashed line gives the empirical relation $\mu_S = V^{-0.0774}$, with the 95% confidence interval (see Supplementary Table 4 in Lucas et al., 2014).

only if relatively small friction coefficients (close to or smaller than the topographic slope) are used in the simulations, whatever the initial dynamics.

Nevertheless, the fact that the initial mechanism has little influence on the travel distance may be true for large collapses only. On May 11, 2010, destabilizations occurred as a succession of 47 successive events (Clouard et al., 2013). Given the estimated 2.1×10^6 m^3 total volume that collapsed during the whole crisis, this suggests an average volume of less than 50,000 m^3 per event. Following Lucas et al. (2014), friction coefficients around $\mu_S = \tan(23°) = 0.42$ are needed to model the propagation of such volumes. In turn, these small granular avalanches stop in the vicinity of the cliff toe, as observed in the field, and do not enter the river bed. In comparison, larger granular flows are modeled with lower friction coefficients (e.g. $\mu_S = \tan(14°) = 0.25$ in our simulations) and have longer runouts (for a review of possible mechanisms enhancing the mobility of large landslides, see e.g. Korup et al., 2013).

To investigate into more details the initiation mechanisms, Discrete Element Methods simulations can be carried out to model explicitly the interactions between blocks (e.g. Chen and Wu, 2018; Do and Wu, 2020; Feng et al., 2021). However, we believe that such models are not necessarily better suited than thin-layer models to simulate the propagation. As a matter of fact, the Samperre cliff is composed of indured pyroclastic deposits that disintegrate rather quickly after the destabilization into sand and boulders. Given the volumes considered (about 1×10^6 m^3 for the large rock avalanches), modeling explicitly each particle in DEM simulations would demand too much computational resources. The explicit modeling of fracture propagation and disintegration is also possible but meets the same computational limitations (Stead and Coggan, 2006).

7.2 Debris flow modeling

7.2.1 Rheology and rheological parameters

In this work we have tested only the Coulmb and Voellmy rheologies. Another possible rheology that could have been investigated (but that is not implemented in SHALTOP) is the combined Darcy-Weisbach and Manning rheology (Chow, 1959;

O'Brien et al., 1993; Jakob et al., 2013):

$$T = \rho n^2 \frac{u^2}{h^{1/3}}, \tag{8}$$

where n is the Manning coefficient. Note that Equation (8) resembles Equation (3) giving the basal stress in the Voellmy rheology. Assuming a Manning coefficient $n = 0.05$ (Jakob et al., 2013), a flow height $h = 5$ m (average flow depth in our simulation), a turbulence coefficent $\xi = 500$ m s^{-2} (as in our simulations), and $g = 9.81$ m s^{-2}, we have:

$$T = 1.5\times10^{-3}\rho u^2 \text{ for the Darcy-Manning rheology,} \tag{9}$$

$$T = 2.0\times10^{-2}\rho u^2 \text{ for the Voellmy rheology.} \tag{10}$$

We may thus expect faster flows with the Darcy-Manning rheology. However, note that Equation (8) is derived empirically for permanent flows in open channels only (Chow, 1959). Thus, we do not believe that the Darcy-Manning rheology is more fitted to debris flow simulations that the Voellmy or Coulomb rheologies.

The Voellmy rheology is commonly used to model fast gravity-driven flows such as snow avalanches and debris flows because Coulomb sometimes fails to reproduce observed velocities (Peruzzetto et al., 2018a). It can indeed yield velocities unrealistically high, as the flow accelerates as long as the topographic slope exceeds the friction coefficient (Kelfoun, 2011). Note that this problem could be the result of the shallow approximation (i. e. hydristatic pressure) that lead to strong overestimation of the velocity (Figure 9b of (Mangeney et al., 2010), Figures 19 and 20 of (Garres-Díaz et al., 2021)). Although, in some cases, the Voellmy rheology allows to better fit observed velocities (e.g. Peruzzetto et al., 2018a), its two parameters can be difficult to constrain. Indeed, several couples (μ_S, ξ) may give similar results.

In the case of the Prêcheur river, we showed that the Coulomb rheology could reproduce both the travel duration and flooded area of the Jun. 19, 2010 DF. Thus, with the data available to characterize this event in particular, there is no clear advantage of using the Voellmy rheology, and thus of introducing a second rheological parameter.

When no calibration data are available, the choice of rheological parameters is more complex. In the case of visco-plastic DFs, rheometry, slump tests and flume tests can be done at the laboratory scale to estimate, in particular, the flow viscosity and yield stress (e.g. Coussot et al., 1998; Remaître et al., 2005; Bouteiller et al., 2021). However, the resulting rheological parameters do not always allow to reproduce observations in thin-layer simulations, because the samples are generally sieved to include only the fine fraction for experimental constraints, and may thus not be representative of the actual DF (Sosio et al., 2007). Besides, viscosity and yield stress depend on solid concentration (Iverson, 2003).

Anyway, in our case, the granulometry of the deposits suggests that the DF dynamics have a frictional mechanical behaviour. To our knowledge, no laboratory experiment allows to estimate the friction coefficient μ_S used to model debris flows in these conditions, with the Coulomb rheology. A basic approach, though, is to consider the slope where the debris flow is expected to stop, and use the corresponding friction coefficient. This rationale helped us define a range of possible values for μ_s before calibration, and was also used for instance by Franco-Ramos et al. (2020) with the Voellmy rheology. It demands, of course, an a priori on the debris flow expected runout, that can be justified by field observations or expert judgment. Thus, in this case, the operational relevance of simulations is not to indicate whether the debris flow will reach a particular location. It is rather to estimate key characteristics of the flow such as travel time or flooded areas, provided the debris flow reaches a given location. Such information are important for hazard assessment.

With the Voellmy rheology, the turbulence coefficient is, by definition, empirical (Salm et al., 1990), and thus must be calibrated. A range of possible values may however be given by the litterature (e.g. Zimmermann et al., 2020).

7.2.2 Erosion processes

As discussed previously, we have not considered entrainment in our simulations. Apart from the influence such a process could have on the DF initiation, we may expect that erosion influences the DF dynamics further downstream as shown in laboratory experiments of granular flows (Mangeney et al., 2010; Farin et al., 2014; Iverson et al., 2011; Mangeney, 2011). In particular, the upper river section above RPRE is narrow and steep-walled, with slopes between 7° and 12°, such that it is prone to bed (from previous lahar deposits) and lateral erosion. The increase of DF volume is difficult to estimate in our case. However, drastic volume increase is sometimes observed in other contexts (e.g., from 150 to 1620 m^3 for the 2000 Tsing Shan debris flow in Hong Kong, Pirulli and Pastor, 2012).

Nevertheless, such processes are difficult to model and constrain. Erosion rate is classically assumed to be proportional to the flow momentum (McDougall and Hungr, 2005; Pirulli and Pastor, 2012), but other studies suggest it is actually inversely proportional to the flow velocity (Iverson, 2012; Lusso et al., 2017, 2020). Bouchut et al. (2008), and later on Iverson (2014), highlight the methodological complexity of deriving a physically based model for erosion, in particular to ensure energy is preserved in the momentum equations (see also Iverson and Ouyang, 2015; Pudasaini and Fischer, 2020). Both with empirical and physically-based erosion laws, simulation results strongly depend on an a priori expert knowledge of erosion areas and erodible thicknesses.

As shown in Section 6.3, the initial mass geometry or source location of DF simulations have a limited influence on simulation results, at least when the DF is initiated in the upper section of the river, above RPRE. Thus, the DF volume increase due to erosion in this section can be accommodated for empirically, in a first approximation, by directly changing the DF initial volume. In the second section of the river that is wider and flatter, we may expect that deposition will prevail over erosion. It may nevertheless not stand true when DFs occur one after another, entraining loose and unconsolidated deposits of previous DFs. To investigate such situations and model DF bulking, it may be necessary to take into account erosion, even empirically.

7.2.3 Overflow hazard

DF simulations provide a first insight on the areas most exposed to overflow hazard. The possibility that DFs overflow the river banks between the bridge and RPRE, or enter adjacent gullies, is a major concern. In an expert report, Quefféléan (2018) suggests that the rocky edge separating the Prêcheur river from the Ravine Démare, a few hundred meters downstream CCPA, could be overflowed (or even destroyed) by high discharge DFs. Although the over-topping of river banks is a highly non-linear phenomenon, with thresholds effects (Mergili et al., 2018; Peruzzetto et al., 2019) that are not easy to predict precisely, such an overflow is reproduced in our *DF_fwd* simulation with Coulomb and $\mu_S = \tan(2°)$. This simulation also suggests that part of the flow may enter the gully between the Prêcheur river and the Ravine Démare (Figure 10c). This possibility had not been considered by Quefféléan (2018), and should be further investigated in future field works.

Analyzing flood hazard in the village is also of prior importance, but its quantification is not easy either. Indeed, flow mobility has competing effects. On the one hand, more material will reach the Prêcheur village when smaller friction coefficients and/or higher turbulence coefficients are used, increasing overflow hazard. On the other hand, low friction coefficients favor the evacuation of debris into the ocean. For instance, in the *DF_2010_1* scenario, when we increase the turbulence coefficient (up to infinite values for the Coulomb rheology), the flooded area on the river right bank expands for $\mu_S = \tan(3°)$ but lessens for $\mu_S = \tan(2°)$ (Figure 9e).

At the mouth of the river, overflows are all the more hard to model as they strongly depend on the river bed filling level, that can vary during a DF because of progressive sediment settling. Such a process is not modeled in SHALTOP where we consider a one-phase flow, with the flowing column stopping at once. Multi-phase shallow water models, such as *D-Claw* (George and Iverson, 2014; Iverson and George, 2014), *r.avaflow* (Mergili et al., 2017; Pudasaini and Mergili, 2019) or *GeoFlow_SPH* (Pastor et al., 2018b), could help investigate such effects. But, as discussed previously, they are more complex to calibrate and the design of appropriate erosion/deposition laws is still an open issue.

Another key physical process that we do not model, but that may be important to asses correctly overflow hazard at the mouth of the river, is the dilution of the DF as it reaches the sea. As we do not have bathymetric data, the altitude in the sea is set to 0 and we let the material flow freely through the grid boundary. Provided bathymetric data is available, the interaction between sea water and the DF can, in theory, be empirically modeled with two-phase or multi-phase models (Pudasaini and Mergili, 2019). We may however expect some process, such as the the transformation of the DF into a turbidity current (Elverhøi et al., 2000), not to be properly simulated. To our knowledge, research has mainly focused on understanding the generation of tsunamis by debris flows (e.g. Walder and Watts, 2003; de Lange et al., 2020), rather than on the influence of debris flow dilution in a large water body on the upstream dynamics. As the Prêcheur village is built around the river mouth, it may be worth investigating this aspect.

7.2.4 Comparison between DF simulations and other documented events

We focused on the modeling of high discharge DFs because their velocity favors the mixing of solid and fluid phases and prevents sediment settling. In turn, the assumption of a homogeneous flow is more acceptable for high discharge DFs than for smaller events, and in particular HFs, where the solid and fluid phases are separated. However, we may wonder if our simulations allow to reproduce empirically and in a first approximation the distribution of flow travel durations between RPRE and CPMA of other documented events. In Figure 15, we compare travel times measured on the 8 strongest lahars (without distinguishing between DFs and HFs) between September 2009 and August 2010 (classified as "strong" or "very strong" by Aubaud et al., 2013, without distinguishing between DFs and HFs), to travel times modeled for the *DF_2010_1* and *DF_2010_2* scenarios with various rheological parameters (μ_S between tan(2°) and tan(4°), and ξ between 100 m s^{-2} and 500 m s^{-2}).

Observed average travel durations decrease for increasing peak FULL values at RPRE (Figure 15a). When the latter are higher than 3000 mV, lahars need no more than 7 min to go from RPRE to CPMA. However, when RPRE FULL records are about 1000 mV, travel durations span from 2 to 15 min. Any further interpretation is difficult because of picking uncertainty: sampling interval is only 1 min and the identification of maximum couples in RPRE and CPMA is sometimes difficult.

However, we could reproduce the same range of travel durations by using different initial conditions and rheological parameters (Figure 15b). High discharges at RPRE (more than 5000 m^3 s^{-1}) are associated to travel durations between RPRE and CPMA below 5 min, while a discharge of 2500 m^3 s^{-1} yields durations spanning from 5 min to 12 min. With the Voellmy rheology, changing rheological parameters only slightly changes the modeled discharge but entails important variations in travel durations (e.g., triangles in Figure 15b). To the contrary, with the Coulomb rheology, a same simulation scenario will produce different discharges depending on the friction coefficient (e.g., triangles with dashed black circles in Figure 15b).

This preliminary analysis is encouraging: even with a simple one-phase thin-layer model and no more than two parameters, we model realistic travel times. However, a more thorough comparison with other recorded DFs and HFs is needed to assess more precisely the capabilities of SHALTOP, and to estimate rheological parameters depending on the lahar (DF or HF) characteristics. This could be done with a catalogue of more recent lahars: their dynamics is better constrained thanks to the

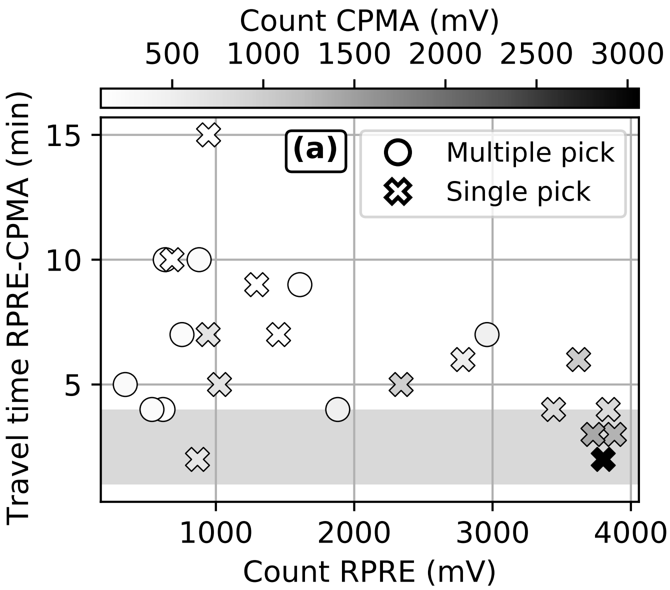

Figure 15. Flow travel durations between RPRE and CPMA deduced from AFMs recordings and simulations. (a) Dephasing between RPRE and CPMA FULL channel maximum, as a function of RPRE FULL channel maximum. Greyscale gives the maximum amplitude recorded on CPMA FULL channel. Picking is done manually for lahars with "strong intensity" between 2009 and 2011, from the database of Aubaud et al. (2013). Crosses: match between RPRE and CPMA FULL maximum is unambiguous. Circles: uncertain pick, with multiple maximums in FULL CPMA possibly matching one maximum in FULL RPRE. (b) Dephasing between maximum discharges at RPRE and CPMA in simulation, as a function of maximum discharge at RPRE. Colorscale gives maximum discharge at CPMA. Symbols give the simulation scenario. Symbols with dashed black contour indicate simulations where the Coulomb rheology is used (Voellmy otherwise). Friction coefficient is $\mu_S = \tan(2°)$, $\mu_S = \tan(3°)$ and $\mu_S = \tan(4°)$. Turbulence coefficients range from 100 to 500 m s^{-2}. Grey patches give observation ranges for the Jun. 19, 2010 DF.

CCPA AFM that was installed in 2014.

8 CONCLUSION

In this work, we have modeled a rock avalanche, and the subsequent remobilization of the deposits as a high discharge debris flow, with a single thin-layer numerical code, SHALTOP. SHALTOP is used empirically, with a maximum of two rheological parameters (Coulomb or Voellmy rheology). We focus on extreme events, and in particular high discharge DFs, in a risk conservative approach. The simplicity of the modeling solution is compensated by an extensive use of field data to define realistic simulation scenarios and calibrate rheological parameters. By doing so, we can reproduce the main characteristics of extreme events, at least in a first approximation. We argue that more complex models may not necessarily yield better results. Although they can simulate more complex processes (such as erosion or variations in solid concentrations), they include more parameters that are difficult to determine, and whose number may improve artificially the quality of back-analysis.

Besides, we show that, in our simulations:

- For similar volumes, successive rock avalanches yield a better match between simulations and seismic signals, but do not change the geometry of the simulated deposits.

- An instantaneous remobilization of the debris reservoir and a simple Coulomb rheology are sufficient to reproduce the main characteristics of a documented high discharge DF.

- For a DF of a given volume, a progressive remobilization of the debris reservoir slows down the DF, in comparison to an instantaneous release.

Our results pave the way to better quantifying flood hazard in the Prêcheur village, by identifying the areas at risk and potential overflows in adjacent gullies. Although we focused on modeling extreme events, we show that our simulated travel durations are consistent with observations for the main lahars (DFs and HFs alike) of 2009 and 2010. Thus, the construction of a simulation database with SHALTOP could also provide first order scaling laws between DF characteristics in the upper and lower parts of the river, which would be useful for real time monitoring. Further work is however needed to assess SHALTOP performance for smaller DFs and HFs, in comparison to observations and other more complex models. Future research could also investigate the relation between lahar initiation, volume and dynamics, and try modeling the continuous transition from a rock avalanche to a DF.

We considered rock avalanches and DFs in a volcanic context, but the sequence of these two kind of events is also relatively common in all mountainous areas (e.g. Walter et al., 2020). The methodology presented in this work can be, supposedly, extended to such contexts.

9 ACKNOWLEDGEMENTS

We thank Janusz Wasowski and two anonymous reviewers for their comments. We gratefully thank the French Ministère de la Transition Ecologique et Solidaire (MTES), the BRGM for funding this work for 2017-2020 as well as the ERC contract ERC-CG-2013-PE10-617472 SLIDEQUAKES and the DEAL Martinique for their contribution. Numerical computations were performed on the S-CAPAD platform, IPGP, France. We also thank the staff of OVSM-IPGP, BRGM Guadeloupe and BRGM Martinique for their contribution to field work and data acquisition. General funding for the Observatoires Volcanologiques et Sismologiques (OVS, IPGP) is provided by IPGP as well as CNRS INSU (Service National d'Observation en Volcanologie, SNOV). The 07/2010 and 08/2018 DEM were derived from LiDAR acquisitions carried out by the Helimap company. The 01/2018 drone overflight of the Samperre Cliff was done by the Carige company. This study contributes to the Université de Paris ANR-18-IDEX-0001 IdEx initiative. This is IPGP contribution 4197.

10 AUTHOR CONTRIBUTION

Conceptualization, Methodology and Validation, M.P., C.L., Y.T., G.G., A.M., A-M.L., A.N., Y.L., J-M.S.; Formal Analysis, Investigation and Visualization M.P.; Resources and Data Curation, M.P, C.L., Y.T., A-M.L., A.N., Y.L., J-M.S., V.C., T.D., S.L.; Writing Original Draft Preparation, M.P.; Writing Review & Editing, M.P., C.L., Y.T., G.G., A.M., A-M.L., A.N., Y.L., B.V., J-M.S., V.C., T.D., F.F., M.M., S.L.,, J-C.K., A.L.F., A.L.,; Supervision, Project Administration, and Funding Acquisition A.M., G.G., C.L., Y.T. A-M.L., B.V., J-C.K., A.L.F., A.L., F.F.

REFERENCES

Aaron, J. and McDougall, S. (2019). Rock avalanche mobility: The role of path material. *Engineering Geology*, page S0013795218319240.

Andreotti, B., Forterre, Y., and Pouliquen, O. (2013). *Granular Media: Between Fluid and Solid*. Cambridge University Press, Cambridge.

Aubaud, C., Athanase, J.-E., Clouard, V., Barras, A.-V., and Sedan, O. (2013). A review of historical lahars, floods, and landslides in the Precheur river catchment (Montagne Pelee volcano, Martinique island, Lesser Antilles). *Bulletin de la Societe Geologique de France*, 184(1-2):137–154.

Baker, J. L., Barker, T., and Gray, J. M. N. T. (2016). A two-dimensional depth-averaged mu(I)-rheology for dense granular avalanches. *Journal of Fluid Mechanics*, 787:367–395.

Bardou, E., Ancey, C., Bonnard, C., and Vulliet, L. (2003). Classification of debris-flow deposits for hazard assessment in alpine areas. In *Debris-Flow Hazards Mitigation : Mechanics, Prediction and Assessment*, volume 2, page 11. Millpress, rickenmann & chen edition.

Bouchut, F., Fernández-Nieto, E., Mangeney, A., and Narbona-Reina, G. (2015). A two-phase shallow debris flow model with energy balance. *ESAIM: Mathematical Modelling and Numerical Analysis*, 49(1):101–140.

Bouchut, F., Fernández-Nieto, E. D., Mangeney, A., and Lagrée, P.-Y. (2008). On new erosion models of Savage–Hutter type for avalanches. *Acta Mechanica*, 199(1-4):181–208.

Bouchut, F., Fernández-Nieto, E. D., Mangeney, A., and Narbona-Reina, G. (2016). A two-phase two-layer model for fluidized granular flows with dilatancy effects. *Journal of Fluid Mechanics*, 801:166–221.

Bouchut, F., Mangeney-Castelnau, A., Perthame, B., and Vilotte, J.-P. (2003). A new model of Saint Venant and Savage–Hutter type for gravity driven shallow water flows. *Comptes Rendus Mathematique*, 336(6):531–536.

Bouchut, F. and Westdickenberg, M. (2004). Gravity driven shallow water models for arbitrary topography. *Communications in Mathematical Sciences*, 2(3):359–389.

Boudon, G., Le Friant, A., Komorowski, J.-C., Deplus, C., and Semet, M. P. (2007). Volcano flank instability in the Lesser Antilles Arc: Diversity of scale, processes, and temporal recurrence. *Journal of Geophysical Research*, 112(B8).

Bouteiller, C. L., Chambon, G., Naaim-Bouvet, F., and Mathys, N. (2021). Hydraulics and rheology of natural hyperconcentrated flows from Draix-Bleone observatory, French Alps. *Journal of Hydraulic Research*, 59(2):181–195.

Brunet, M., Moretti, L., Le Friant, A., Mangeney, A., Fernández Nieto, E. D., and Bouchut, F. (2017). Numerical simulation of the 30–45 ka debris avalanche flow of Montagne Pelée volcano, Martinique: From volcano flank collapse to submarine emplacement. *Natural Hazards*, 87(2):1189–1222.

Chen, K.-T. and Wu, J.-H. (2018). Simulating the failure process of the Xinmo landslide using discontinuous deformation analysis. *Engineering Geology*, 239:269–281.

Chow, V. T. (1959). *Open-Channel Hydraulics*. McGraw Hill Book Company.

Clouard, V., Athanase, J.-E., and Aubaud, C. (2013). Physical characteristics and triggering mechanisms of the 2009-2010 landslide crisis at Montagne Pelee volcano, Martinique: Implication for erosional processes and debris-flow hazards. *Bulletin de la Societe Geologique de France*, 184(1-2):155–164.

Cole, S. E., Cronin, S. J., Sherburn, S., and Manville, V. (2009). Seismic signals of snow-slurry lahars in motion: 25 September

2007, Mt Ruapehu, New Zealand. *Geophysical Research Letters*, 36(9).

Coussot, P., Lailgle, D., Arattano, M., Deganutti, A., and Marchi, L. (1998). Direct determination of rheological characteristics of debris flow. *Amercian Society of Civil Engineers*, 124(8).

Coussot, P. and Meunier, M. (1996). Recognition, classification and mechanical description of debris flows. *Earth-Science Reviews*, 40(3-4):209–227.

de Lange, S., Santa, N., Pudasaini, S., Kleinhans, M., and de Haas, T. (2020). Debris-flow generated tsunamis and their dependence on debris-flow dynamics. *Coastal Engineering*, 157:103623.

Delannay, R., Valance, A., Mangeney, A., Roche, O., and Richard, P. (2017). Granular and particle-laden flows: From laboratory experiments to field observations. *Journal of Physics D: Applied Physics*, 50(5):053001.

Do, T. N. and Wu, J.-H. (2020). Simulating a mining-triggered rock avalanche using DDA: A case study in Nattai North, Australia. *Engineering Geology*, 264:105386.

Dumaisnil, C., Thouret, J.-C., Chambon, G., Doyle, E. E., Cronin, S. J., and Surono (2010). Hydraulic, physical and rheological characteristics of rain-triggered lahars at Semeru volcano, Indonesia. *Earth Surface Processes and Landforms*, 35(13):1573–1590.

Durán, O., Andreotti, B., and Claudin, P. (2012). Numerical simulation of turbulent sediment transport, from bed load to saltation. *Physics of Fluids*, 24(10):103306.

Elverhøi, A., Harbitz, C., Dimikis, P., Mohrig, D., Marl, J., and Parker, G. (2000). On the Dynamics of Subaqueous Debris Flows. *Oceanography*, 13(3):109–117.

Faccanoni, G. and Mangeney, A. (2012). Exact solution for granular flows: EXACT SOLUTION FOR GRANULAR FLOWS. *International Journal for Numerical and Analytical Methods in Geomechanics*, 37(10):1408–1433.

Farin, M., Mangeney, A., and Roche, O. (2014). Fundamental changes of granular flow dynamics, deposition, and erosion processes at high slope angles: Insights from laboratory experiments. *Journal of Geophysical Research: Earth Surface*, 119(3):504–532.

Favreau, P., Mangeney, A., Lucas, A., Crosta, G., and Bouchut, F. (2010). Numerical modeling of landquakes: Landslides and seismic waves. *Geophysical Research Letters*, 37(15):L15305.

Feng, Z.-Y., Lu, Y.-R., and Shen, Z.-R. (2021). A numerical simulation of seismic signals of coseismic landslides. *Engineering Geology*, 289:106191.

Franco-Ramos, O., Ballesteros-Cánovas, J. A., Figueroa-García, J. E., Vázquez-Selem, L., Stoffel, M., and Caballero, L. (2020). Modelling the 2012 Lahar in a Sector of Jamapa Gorge (Pico de Orizaba Volcano, Mexico) Using RAMMS and Tree-Ring Evidence. *Water*, 12(2):333.

Frimberger, T., Andrade, S. D., Weber, S., and Krautblatter, M. (2021). Modelling future lahars controlled by different volcanic eruption scenarios at Cotopaxi (Ecuador) calibrated with the massively destructive 1877 lahar. *Earth Surface Processes and Landforms*, 46(3):680–700.

Garres-Díaz, J., Fernández-Nieto, E. D., Mangeney, A., and Morales de Luna, T. (2021). A Weakly Non-hydrostatic Shallow Model for Dry Granular Flows. *Journal of Scientific Computing*, 86(2):25.

GDR MiDi (2004). On dense granular flows. *The European Physical Journal E*, 14(4):341–365.

George, D. L. and Iverson, R. M. (2014). A depth-averaged debris-flow model that includes the effects of evolving dilatancy. II. Numerical predictions and experimental tests. *Proceedings of the Royal Society A: Mathematical, Physical and Engineering*

Sciences, 470(2170):20130820.

Germa, A., Quidelleur, X., Lahitte, P., Labanieh, S., and Chauvel, C. (2011). The K–Ar Cassignol–Gillot technique applied to western Martinique lavas: A record of Lesser Antilles arc activity from 2Ma to Mount Pelée volcanism. *Quaternary Geochronology*, 6(3-4):341–355.

Gray, J., Wieland, M., and Hutter, K. (1999). Gravity-driven free surface flow of granular avalanches over complex basal topography. *Proceedings of the Royal Society of London A: Mathematical, Physical and Engineering Sciences*, 455:1841–1874.

Gray, J. M. N. T., Tai, Y.-C., and Noelle, S. (2003). Shock waves, dead zones and particle-free regions in rapid granular free-surface flows. *Journal of Fluid Mechanics*, 491:161–181.

Guimpier, A., Conway, S. J., Mangeney, A., Lucas, A., Mangold, N., Peruzzetto, M., Pajola, M., Lucchetti, A., Munaretto, G., Sæmundsson, T., Johnsson, A., Le Deit, L., Grindrod, P., Davis, J., Thomas, N., and Cremonese, G. (2021). Dynamics of recent landslides (<20 My) on Mars: Insights from high-resolution topography on Earth and Mars and numerical modelling. *Planetary and Space Science*, 206:105303.

Hibert, C., Mangeney, A., Grandjean, G., and Shapiro, N. M. (2011). Slope instabilities in Dolomieu crater, Réunion Island: From seismic signals to rockfall characteristics. *Journal of Geophysical Research*, 116(F4).

Hu, M., Liu, M. B., Xie, M. W., and Liu, G. R. (2015). Three-dimensional run-out analysis and prediction of flow-like landslides using smoothed particle hydrodynamics. *Environmental Earth Sciences*, 73(4):1629–1640.

Hungr, O., Leroueil, S., and Picarelli, L. (2014). The Varnes classification of landslide types, an update. *Landslides*, 11(2):167–194.

Hungr, O., Morgenstern, N., and Wong, H. (2007). Review of benchmarking exercise on landslide debris runout and mobility modelling. In *Proceedingd of The 2007 International Forum on Landdslide Disaster Management*. Ho & Li.

INSEE (2020). Comparateur de territoire, commune du Prêcheur (97219). https://www.insee.fr/fr/statistiques/1405599?geo=COM-97219.

Iverson, R. M. (2003). The debris-flow rheology myth. In *3rd International Conference on Debris-Flow Hazards Mitigation: Mechanics, Prediction, and Assessment*, volume 1, pages 303–314.

Iverson, R. M. (2012). Elementary theory of bed-sediment entrainment by debris flows and avalanches. *Journal of Geophysical Research: Earth Surface*, 117(F3):n/a–n/a.

Iverson, R. M. (2014). Debris flows: Behaviour and hazard assessment. *Geology Today*, 30(1):15–20.

Iverson, R. M. and George, D. L. (2014). A depth-averaged debris-flow model that includes the effects of evolving dilatancy. I. Physical basis. *Proceedings of the Royal Society A: Mathematical, Physical and Engineering Sciences*, 470(2170):20130819.

Iverson, R. M. and Ouyang, C. (2015). Entrainment of bed material by Earth-surface mass flows: Review and reformulation of depth-integrated theory. *Reviews of Geophysics*, 53(1):27–58.

Iverson, R. M., Reid, M. E., Logan, M., LaHusen, R. G., Godt, J. W., and Griswold, J. P. (2011). Positive feedback and momentum growth during debris-flow entrainment of wet bed sediment. *Nature Geoscience*, 4(2):116–121.

Jakob, M., McDougall, S., Weatherly, H., and Ripley, N. (2013). Debris-flow simulations on Cheekye River, British Columbia. *Landslides*, 10(6):685–699.

Jones, R., Manville, V., and Andrade, D. (2015). Probabilistic analysis of rain-triggered lahar initiation at Tungurahua volcano. *Bulletin of Volcanology*, 77(8):68.

Jop, P., Forterre, Y., and Pouliquen, O. (2006). A constitutive law for dense granular flows. *Nature*, 441(7094):727–730.

Kelfoun, K. (2011). Suitability of simple rheological laws for the numerical simulation of dense pyroclastic flows and long-runout volcanic avalanches. *Journal of Geophysical Research*, 116(B8).

Korup, O., Schneider, D., Huggel, C., and Dufresne, A. (2013). Long-Runout Landslides. In *Treatise on Geomorphology*, pages 183–199. Elsevier.

Kuo, C. Y., Tai, Y. C., Bouchut, F., Mangeney, A., Pelanti, M., Chen, R. F., and Chang, K. J. (2009). Simulation of Tsaoling landslide, Taiwan, based on Saint Venant equations over general topography. *Engineering Geology*, 104(3):181–189.

LaHusen, R. (2005). Acoustic Flow Monitor System - User Manual. USGS Numbered Series 2002-429, Geological Survey (U.S.).

LaHusen, R. G. (1998). Detecting debris flows using ground vibrations. USGS Numbered Series 236-96, U.S. Geological Survey.

Laigle, D. and Macabies, P. (2010). Compte rendu de la mission du 14 au 16 décembre 2010. Technical report, Cemagref/ONF-RTM/DIREN.

Lalubie, G. (2013). Les Lahars et les laves torrentielles historiques aux Antilles françaises : un risque hydro-volcano-géomorphologique majeur. *Physio-Géo. Géographie physique et environnement*, 7(Volume 7):83–109.

Lavigne, F., Thouret, J. C., Voight, B., Suwa, H., and Sumaryono, A. (2000). Lahars at Merapi volcano, Central Java: An overview. *Journal of Volcanology and Geothermal Research*, 100(1):423–456.

Le Friant, A., Boudon, G., Deplus, C., and Villemant, B. (2003). Large-scale flank collapse events during the activity of Montagne Pelée, Martinique, Lesser Antilles. *Journal of Geophysical Research: Solid Earth*, 108(B1).

Lefebvre-Lepot, A., Merlet, B., and Nguyen, T. N. (2015). An accurate method to include lubrication forces in numerical simulations of dense Stokesian suspensions. *Journal of Fluid Mechanics*, 769:369–386.

Leonardi, A., Wittel, F. K., Mendoza, M., and Herrmann, H. J. (2014). Coupled DEM-LBM method for the free-surface simulation of heterogeneous suspensions. *Computational Particle Mechanics*, 1(1):3–13.

Levy, C., Mangeney, A., Bonilla, F., Hibert, C., Calder, E. S., and Smith, P. J. (2015). Friction weakening in granular flows deduced from seismic records at the Soufrière Hills Volcano, Montserrat. *Journal of Geophysical Research: Solid Earth*, 120(11):7536–7557.

Lucas, A. and Mangeney, A. (2007). Mobility and topographic effects for large Valles Marineris landslides on Mars. *Geophysical Research Letters*, 34(10).

Lucas, A., Mangeney, A., and Ampuero, J. P. (2014). Frictional velocity-weakening in landslides on Earth and on other planetary bodies. *Nature Communications*, 5.

Lucas, A., Mangeney, A., Bouchut, F., Bristeau, M.-O., and Mège, D. (2007). Benchmarking Exercises for Granual Flows. In *The 2007 International Forum on Landslide Disaster Management*, Hong Kong. Ho & Li.

Lusso, C., Bouchut, F., Ern, A., and Mangeney, A. (2017). A Free Interface Model for Static/Flowing Dynamics in Thin-Layer Flows of Granular Materials with Yield: Simple Shear Simulations and Comparison with Experiments. *Applied Sciences*, 7(4):386.

Lusso, C., Bouchut, F., Ern, A., and Mangeney, A. (2020). Explicit solutions to a free interface model for the static/flowing transition in thin granular flows. *ESAIM: Mathematical Modelling and Numerical Analysis*.

Mangeney, A. (2011). Landslide boost from entrainment. *Nature Geoscience*, 4(2):77–78.

Mangeney, A., Bouchut, F., Thomas, N., Vilotte, J. P., and Bristeau, M. O. (2007a). Numerical modeling of self-channeling granular flows and of their levee-channel deposits. *Journal of Geophysical Research*, 112(F2).

Mangeney, A., Heinrich, P., and Roche, R. (2000). Analytical Solution for Testing Debris Avalanche Numerical Models. *Pure and Applied Geophysics*, 157(6-8):1081–1096.

Mangeney, A., Roche, O., Hungr, O., Mangold, N., Faccanoni, G., and Lucas, A. (2010). Erosion and mobility in granular collapse over sloping beds. *Journal of Geophysical Research*, 115(F3).

Mangeney, A., Tsimring, L. S., Volfson, D., Aranson, I. S., and Bouchut, F. (2007b). Avalanche mobility induced by the presence of an erodible bed and associated entrainment. *Geophysical Research Letters*, 34(22).

Mangeney-Castelnau, A., Bouchut, F., Vilotte, J. P., Lajeunesse, E., Aubertin, A., and Pirulli, M. (2005). On the use of Saint Venant equations to simulate the spreading of a granular mass: Numerical simulation of granular spreading. *Journal of Geophysical Research: Solid Earth*, 110(B9).

Marcial, S., Melosantos, A. A., Hadley, K. C., LaHusen, R. G., and Marso, J. A. (1996). Instrumental Lahar Monitoring at Mount Pinatubo. In *Fire and Mud: Eruptions and Lahars of Mount Pinatubo, Philippines*, page 32. University of Washington Press, c.g. newhall and r.s. punongbayan edition.

Mathon, C. and Barras, A. (2010). Risque d'occurence de lave torrentielle dans la rivière du Prêcheur suite à l'éboulement du 11 Mai 2010. Rapport d'expertise BRGM/RP - 58697-FR, BRGM.

McDougall, S. (2017). 2014 Canadian Geotechnical Colloquium: Landslide runout analysis — current practice and challenges. *Canadian Geotechnical Journal*, 54(5):605–620.

McDougall, S. and Hungr, O. (2005). Dynamic modelling of entrainment in rapid landslides. *Canadian Geotechnical Journal*, 42(5):1437–1448.

Mergili, M., Fischer, J.-T., Krenn, J., and Pudasaini, S. P. (2017). R.avaflow v1, an advanced open source computational framework for the propagation and interaction of two-phase mass flows. *Geoscientific Model Development Discussions*, pages 1–30.

Mergili, M., Frank, B., Fischer, J.-T., Huggel, C., and Pudasaini, S. P. (2018). Computational experiments on the 1962 and 1970 landslide events at Huascarán (Peru) with r.avaflow: Lessons learned for predictive mass flow simulations. *Geomorphology*, 322:15–28.

Meunier, M. (1999). *Les torrents du Nord-Ouest de la Martinique. Hydrologie des crues, érosion, hydraulique et dynamique torrentielles - Collectif*. Number 24 in Equipements pour l'eau et l'environnement. Cemagref.

Moretti, L., Allstadt, K., Mangeney, A., Capdeville, Y., Stutzmann, E., and Bouchut, F. (2015). Numerical modeling of the Mount Meager landslide constrained by its force history derived from seismic data. *Journal of Geophysical Research: Solid Earth*, 120(4):2579–2599.

Moretti, L., Mangeney, A., Capdeville, Y., Stutzmann, E., Huggel, C., Schneider, D., and Bouchut, F. (2012). Numerical modeling of the Mount Steller landslide flow history and of the generated long period seismic waves. *Geophysical Research Letters*, 39(16):n/a–n/a.

Moretti, L., Mangeney, A., Walter, F., Capdeville, Y., Bodin, T., Stutzmann, E., and Le Friant, A. (2020). Constraining landslide characteristics with Bayesian inversion of field and seismic data. *Geophysical Journal International*, 221(2):1341–1348.

Nachbaur, A., Legendre, Y., Lombard, M., and Dewez, T. (2019). Caractérisation géologique et identification des mécanismes d'instabilité de la falaise Samperre. Rapport Final RP-68564-FR, BRGM.

O'Brien, J. S., Julien, P. Y., and Fullerton, W. T. (1993). Two-dimensional water flood and mudflow simulation. *Journal of hydraulic engineering*, 119(2):244–261.

OVSM-IPGP (2020). Bulletin mensuel de l'Observatoire Volcanologique et Sismologique de Martinique. Technical Report 2020-03, IPGP.

Pastor, M., Blanc, T., and Pastor, M. (2009). A depth-integrated viscoplastic model for dilatant saturated cohesive-frictional fluidized mixtures: Application to fast catastrophic landslides. *Journal of Non-Newtonian Fluid Mechanics*, 158(1-3):142–153.

Pastor, M., Quecedo, M., González, E., Herreros, M. I., Merodo, J. A. F., and Mira, P. (2004). Simple Approximation to Bottom Friction for Bingham Fluid Depth Integrated Models. *Journal of Hydraulic Engineering*, 130(2):149–155.

Pastor, M., Soga, K., McDougall, S., and Kwan, J. S. H. (2018a). Review of Benchmarking Exercise on Landslide Runout Analysis 2018. *Hong Kong*, page 65.

Pastor, M., Yague, A., Stickle, M., Manzanal, D., and Mira, P. (2018b). A two-phase SPH model for debris flow propagation. *International Journal for Numerical and Analytical Methods in Geomechanics*, 42(3):418–448.

Peruzzetto, M., Komorowski, J.-C., Friant, A. L., Rosas-Carbajal, M., Mangeney, A., and Legendre, Y. (2019). Modeling of partial dome collapse of La Soufrière of Guadeloupe volcano: Implications for hazard assessment and monitoring. *Scientific Reports*, 9(1):1–15.

Peruzzetto, M., Mangeney, A., Bouchut, F., Grandjean, G., Levy, C., Thiery, Y., and Lucas, A. (2021). Topography curvature effects in thin-layer models for gravity-driven flows without bed erosion. *Journal of Geophysical Research: Earth Surface*, page e2020JF005657.

Peruzzetto, M., Mangeney, A., Grandjean, G., Levy, C., Thiery, Y., and Bouchut, F. (2018a). Back-analysis of a rock avalanche and a debris flow with the SHALTOP code. In *Proceedings of the Second JTC1 Workshop on Triggering and Propagation of Rapid Flow-like Landslides*, page 4, Hong Kong.

Peruzzetto, M., Mangeney, A., Levy, C., Thiery, Y., Grandjean, G., Kelfoun, K., and Bouchut, F. (2018b). Analysis of curvature effects for frictional rheologies in thin-layer depth-averaged flow propagation models. In *EGU, Mechanics of Mass Flows, Poster*.

Pirulli, M. and Mangeney, A. (2008). Results of Back-Analysis of the Propagation of Rock Avalanches as a Function of the Assumed Rheology. *Rock Mechanics and Rock Engineering*, 41(1):59–84.

Pirulli, M. and Pastor, M. (2012). Numerical study on the entrainment of bed material into rapid landslides. *Géotechnique*, 62(11):959–972.

Pudasaini, S. P. and Fischer, J.-T. (2020). A mechanical model for phase separation in debris flow. *International Journal of Multiphase Flow*, 129:103292.

Pudasaini, S. P. and Mergili, M. (2019). A Multi-Phase Mass Flow Model. *Journal of Geophysical Research: Earth Surface*, 124(12):2920–2942.

Queffélean, Y. (2018). Mission d'expertise ONF-RTM sur les lahars du Prêcheur. Appui tehcnique DGPR, ONF-RTM.

Remaître, A., Malet, J.-P., Maquaire, O., Ancey, C., and Locat, J. (2005). Flow behaviour and runout modelling of a complex debris flow in a clay-shale basin. *Earth Surface Processes and Landforms*, 30(4):479–488.

Rickenmann, D. (1999). Empirical Relationships for Debris Flows. *Natural Hazards*, 19(1):47–77.

Salm, B. (1993). Flow, flow transition and runout distances of flowing avalanches. *Annals of Glaciology*, 18.

Salm, B., Burkard, A., and Gubler, H. U. (1990). *Berechnung von Fliesslawinen: eine Anleitung fuer Praktiker mit Beispielen*. Eidgenössische Institut für Schnee- und Lawinenforschung, Weissfluhjoch/Davos.

Savage, S. B. and Hutter, K. (1989). The motion of a finite mass of granular material down a rough incline. *Journal of Fluid Mechanics*, 199(-1):177.

Sosio, R., Crosta, G. B., and Frattini, P. (2007). Field observations, rheological testing and numerical modelling of a debris-flow event. *Earth Surface Processes and Landforms*, 32(2):290–306.

Sosio, R., Crosta, G. B., and Hungr, O. (2012). Numerical modeling of debris avalanche propagation from collapse of volcanic edifices. *Landslides*, 9(3):315–334.

Stead, D. and Coggan, J. (2006). Numerical modeling of rock slopes using a total slope failure approach. In Evans, S. G., Mugnozza, G. S., Strom, A., and Hermanns, R. L., editors, *Landslides from Massive Rock Slope Failure*, NATO Science Series, pages 129–138, Dordrecht. Springer Netherlands.

Thouret, J. C., Antoine, S., Magill, C., and Ollier, C. (2020). Lahars and debris flows: Characteristics and impacts. *Earth-Science Reviews*, 201:103003.

Vallance, J. W. and Iverson, R. M. (2015). Lahars and Their Deposits. In *The Encyclopedia of Volcanoes*, pages 649–664. Elsevier.

Walder, J. S. and Watts, P. (2003). Evaluating Tsunami Hazards From Debris Flows. In Locat, J., Mienert, J., and Boisvert, L., editors, *Submarine Mass Movements and Their Consequences: 1st International Symposium*, Advances in Natural and Technological Hazards Research, pages 155–162. Springer Netherlands, Dordrecht.

Walter, F., Amann, F., Kos, A., Kenner, R., Phillips, M., de Preux, A., Huss, M., Tognacca, C., Clinton, J., Diehl, T., and Bonanomi, Y. (2020). Direct observations of a three million cubic meter rock-slope collapse with almost immediate initiation of ensuing debris flows. *Geomorphology*, 351:106933.

Windows-Yule, C. R. K., Tunuguntla, D. R., and Parker, D. J. (2016). Numerical modelling of granular flows: A reality check. *Computational Particle Mechanics*, 3(3):311–332.

Wu, J.-H. and Hsieh, P.-H. (2021). Simulating the postfailure behavior of the seismically- triggered Chiu-fen-erh-shan landslide using 3DEC. *Engineering Geology*, 287:106113.

Yamada, M., Mangeney, A., Matsushi, Y., and Matsuzawa, T. (2018). Estimation of dynamic friction and movement history of large landslides. *Landslides*, 15(10):1963–1974.

Yan, Y., Cui, Y., Guo, J., Hu, S., Wang, Z., and Yin, S. (2020). Landslide reconstruction using seismic signal characteristics and numerical simulations: Case study of the 2017 “6.24” Xinmo landslide. *Engineering Geology*, 270:105582.

Zhao, J. and Shan, T. (2013). Coupled CFD–DEM simulation of fluid–particle interaction in geomechanics. *Powder Technology*, 239:248–258.

Zimmermann, F., McArdell, B. W., Rickli, C., and Scheidl, C. (2020). 2D Runout Modelling of Hillslope Debris Flows, Based on Well-Documented Events in Switzerland. *Geosciences*, 10(2):70.